

Robust and fast backbone tracking via phase-locked loops

Patrick Hippold¹, Maren Scheel¹, Ludovic Renson² Malte Krack¹

¹ *University of Stuttgart, GERMANY*

² *Imperial College London, UK*

Abstract

Phase-locked loops are commonly used for shaker-based backbone tracking of nonlinear structures. The state of the art is to tune the control parameters by trial and error. In the present work, an approach is proposed to make backbone tracking much more robust and faster. A simple PI controller is proposed, and closed-form expressions for the gains are provided that lead to an optimal settling of the phase transient. The required input parameters are obtained from a conventional shaker-based linear modal test, and an open-loop sine test at a single frequency and level. For phase detection, an adaptive filter based on the LMS algorithm is used, which is shown to be superior to the synchronous demodulation commonly used. Once the phase has locked, one can directly take the next step along the backbone, eliminating the hold times. The latter are currently used for recording the steady state, and to estimate Fourier coefficients in the post-process, which becomes unnecessary since the adaptive filter yields a highly accurate estimation at runtime. The excellent performance of the proposed approach is demonstrated for a doubly clamped beam undergoing bending-stretching coupling leading to a 20 percent shift of the lowest modal frequency. Even for fixed control parameters, designed for the linear regime, only about 100 periods are needed per backbone point, also in the nonlinear regime. This is much faster than what has been reported in the literature so far.

Keywords: phase resonance, PLL, NNM, force appropriation

List of symbols

Time, frequency, phase

t	time
Ω	frequency
τ	phase

Excitation and response

u	voltage
U	voltage amplitude
f	applied force
F	Fourier coefficient of f
q_{ex}	drive point displacement
Q	Fourier coefficient of q_{ex}

Exciter physical model

i	current
R	resistance
G	electromotive force constant
k_{ex}	mechanical exciter stiffness
d_{ex}	mechanical exciter damping
m_{ex}	moving exciter mass

Structure physical model

\mathbf{q}	vector of generalized coordinates
\mathbf{M}	mass matrix
\mathbf{g}	restoring and damping forces
\mathbf{e}_{ex}	applied force direction

Plant modal model

ω	modal frequency
D	modal damping ratio
$\boldsymbol{\varphi}$	mass-normalized modal deflection shape
a	modal amplitude
ϑ	phase shift
δ_{p}	decay rate of plant
δ_{s}	decay rate of structure under test
μ_{ex}	mass ratio exciter/structural mode

Adaptive filter

H	harmonic truncation order
ω_{LP}	low-pass filter cutoff frequency

Controller

Ω_{ini}	initial frequency of phase-locked loop
ε	phase shift error
ε_{tol}	tolerance specified for ε
k_{p}	gain of proportional controller part
k_{i}	gain of integral controller part
I_{ε}	integral state of phase controller

Linearized state space model

\mathbf{z}	state vector
\mathbf{A}_0	matrix of linearized dynamical system
Υ	constant of plant
λ	eigenvalue

Constants

i	imaginary unit
e	Euler number

Annotations

$\dot{\square}$	derivative with respect to t
$\bar{\square}$	non-dimensionalized with ω_{LP}
\square'	derivative with respect to \bar{t}
$\tilde{\square}$	including exciter effects
$\hat{\square}$	estimation via adaptive filter
$\square^{(h)}$	h -th harmonic
\square_{ex}	at drive point/of the exciter
\square_{lin}	linear(-ized)
\square_{R}	real part
\square_{I}	imaginary part
$\Delta\square$	deviation from fixed point

1. Introduction

The goal of the present work is to achieve a fast and robust tracking of the phase-resonant backbone curve of nonlinear structures, by a systematic design of the phase-locked loop feedback controller. To motivate the problem setting, an overview is given in the following on the main use cases of phase resonance testing. Then, different means of achieving phase resonance are discussed, including the use of phase-locked loops. Subsequently, the state of the art of the design of phase-locked loops for vibration testing is reviewed. Finally, the outline of the present work is described.

What is phase resonance testing and what is it used for?

Phase resonance testing is mainly used for the identification of modal properties, both in the linear and in the nonlinear case. In the linear case, the approach is commonly referred to as tuned-sinusoidal

or force appropriation (vibration) testing, and it is commonly used to separate modes with closely-spaced frequencies. Here, besides finding the appropriate frequency, the key challenge is to determine an appropriate force pattern (multi-shaker testing) to bring the response into phase resonance at each exciter location, and thus to isolate the individual modes.

Phase resonance testing is also well-known for its ability to investigate (weakly) nonlinear behavior [1]. Atkins et al. [2] showed that a multi-harmonic forcing is theoretically needed in the nonlinear case. Peeters et al. [3, 4] revisited [2] and concluded that single-point mono-harmonic forcing often permits a good isolation of a nonlinear mode, which is an important finding from a practical perspective. A requirement is that damping must be light and the modal frequency must be well-separated (there are no strong modal interactions). It is useful to note that there are different definitions of nonlinear modes. The goal of [3, 4] was to identify a Nonlinear Normal Mode, which is defined a family of periodic motions of the underlying conservative autonomous (unforced-undamped) system. A definition of nonlinear modes that explicitly accounts for (possibly nonlinear) dissipation is the Extended Periodic Motion Concept [5]. To isolate such a mode, the phase-resonant backbone (forced-damped configuration) should be tracked as shown in [6, 7]. For finite damping and closely-spaced modes, the backbone of the unforced-undamped system may deviate considerably from the phase-resonant backbone [8]. Besides the identification of amplitude-dependent modal properties, backbone tracking can be useful to uncover isolated frequency response branches, as shown numerically [9] and experimentally [10].

How to achieve phase resonance? What are phase-locked loops?

To achieve phase resonance, manual tuning of the excitation frequency was used in [4]. As an alternative, this can be achieved using feedback control. A simple example is a velocity feedback loop. Here, the velocity is measured and fed back (via a gain) to the structure under test¹. In the case of velocity feedback, it is not trivial to select the mode to be driven into resonance. To enable a mode selection under a single exciter location, one can acquire the velocity at multiple locations, and include a modal filter into the feedback loop [13].

Two alternatives to velocity feedback are Control-Based Continuation and the use of phase-locked loops. Compared to velocity feedback, both techniques permit an easier mode selection, and do not require that the response is measured at multiple locations. An important benefit of Control-Based Continuation is its robustness; its most important downside is its inherently iterative character [14, 15]. Phase-locked loops, on the other hand, do not require any iterations, so they have the potential for faster backbone tracking, and this is why they are the focus of the present work. Remarkably, phase resonance testing using a phase-locked loop was already applied in the 1970s to identify natural frequencies of biological tissue [16]. Another common application is fatigue testing of MEMS resonators, where the natural frequency varies with time as the crack grows, and the phase-locked loop permits to maintain resonant operation [17]. Phase-locked loops are well-known in electrical and control engineering, and they recently gained popularity for nonlinear vibration testing. A phase-locked loop adjusts the frequency input to the structure under test until a specified phase lag of the response is reached. Besides phase-resonance testing, phase-locked loops are useful also for frequency response testing, where phase control can increase robustness and even obtain coexisting frequency responses (including those that are unstable under open-loop conditions) [11].

What is the state of the art design of phase-locked loops for vibration testing?

Synchronous demodulation (also known as homodyne detection) is by far the most popular means of estimating (or detecting) the phase lag during phase-controlled vibration testing [18, 13]. The input signal (force or response) is multiplied by the sine / cosine of the instantaneous phase. The latter is obtained as the integral of the frequency output of the controller. By applying a low-pass filter, one obtains an estimate of the sine / cosine Fourier coefficient of the signal. In earlier works, the sign of the signal

¹In some cases, the sign of the velocity is taken before it is fed back [11]. However, the sign function introduces higher harmonics and is sensitive to noise. This may distort the resonant dynamics severely compared to a mono-harmonic excitation, especially if the structure does not behave like a single-degree-of-freedom system [12].

was used instead of the signal itself within the phase detector [19, 6]. This might permit simpler digital implementations, and inherently makes the output level independent of the input signal level [20]. However, it usually performs poorly for phase controlled nonlinear vibration testing, since it is highly sensitive to noise and higher harmonics in the signal. Denis et al. [18] introduced separate phase detectors for force and response, and use the two-argument arctangent to compute the phase lag, which also ensures an output level independent of the input. In the present work, an adaptive filter based on the LMS algorithm [21] is used for phase detection, and more generally, for Fourier decomposition. This is commonly used to remove periodic disturbances from a given signal (adaptive notch filter). In the present context, the filtering property of the LMS algorithm is not used, but the fact that it gives a steady-flow estimate of the discrete Fourier transform [22] is particularly suitable for phase and amplitude control tasks within nonlinear vibration testing. It was introduced already by Abeloos et al. [23] to this context, and found superior to synchronous demodulation in [24].

In the context of vibration testing based on phase-locked loops, simple controllers are commonly used (integral, proportional-integral, or proportional-integral-derivative controllers). A stability condition was established for the case of a pure integral controller in [25, 26, 18], and for a proportional-integral-derivative controller in [24]. For this purpose, the plant was modeled as a linear single-degree-of-freedom system [25], with an additional cubic spring [26, 18], or with a more generic nonlinear term [24]. In all those studies, an averaging formalism was used, and the asymptotic behavior around the locked state was considered. For the case of a pure integral controller, a maximum integral gain was established, beyond which the closed loop diverges [25, 26, 18]. This limit depends mainly on the plant damping and the cutoff frequency of the loop filter (within the phase detector), and was found to be independent of the cubic spring [26, 18]. It should be emphasized that the asymptotic stability is only a necessary criterion for a good controller design, and it does not say anything about the robustness or the duration of the settling time. It was observed that an additional proportional gain reduces the settling time down to a certain limit value [19]. In all studies on vibration testing known today, the phase-locked loop parameters were set in a strictly heuristic way.

What alternatives are available for backbone tracking?

Techniques have also been proposed to identify backbone curves, or more specifically, amplitude-dependent modal frequencies and damping ratios, from the free decay (ring down response), see e.g. [27, 28, 29]. If the initial excitation is applied via an impact hammer, the response is generally comprised of multiple modes, and an accurate estimation of individual backbones can only be expected in the rather weakly nonlinear regime, see e.g. [30]. If the initial excitation is provided by a shaker, instantaneously switching off the excitation (e.g. by detaching structure and stinger) without distorting the dynamics of interest is very difficult or even impossible (e.g. in the case of base excitation).

Instead of directly tracking the phase-resonant backbone curve, one can test the frequency-response surface (or manifold) in the space spanned by frequency, response amplitude, excitation amplitude and response-excitation phase lag. The most common ways to do this are to step the frequency while keeping the response amplitude at a target value via feedback control (Response Controlled stepped-sine Testing), see e.g. [31], or to keep the frequency constant while stepping the target value for the response amplitude, to generate so-called S-curves, see e.g. [15]. From the gathered data points, the backbone curve can be obtained by interpolation. Those techniques collect data that is unnecessary when focusing on backbone curves alone. More data commonly means longer test duration, and since the goal of the present work is to obtain the backbone quickly, the focus is placed on direct backbone tracking.

Outline of the present work

In the present work, for the first time, a systematic design approach for backbone tracking using a phase-locked loop is proposed. The goal is to develop an approach that is widely applicable, easy to implement, and requires minimal prior knowledge of the system. In Section 2, the problem setting is formulated. The theory behind the proposed solution approach is described in Section 3. An algorithmic summary of the proposed approach and practical recommendations are given in Section 4. Numerical validation and an experimental assessment are presented in Section 5 and Section 6, respectively. Concluding remarks are made in Section 7.

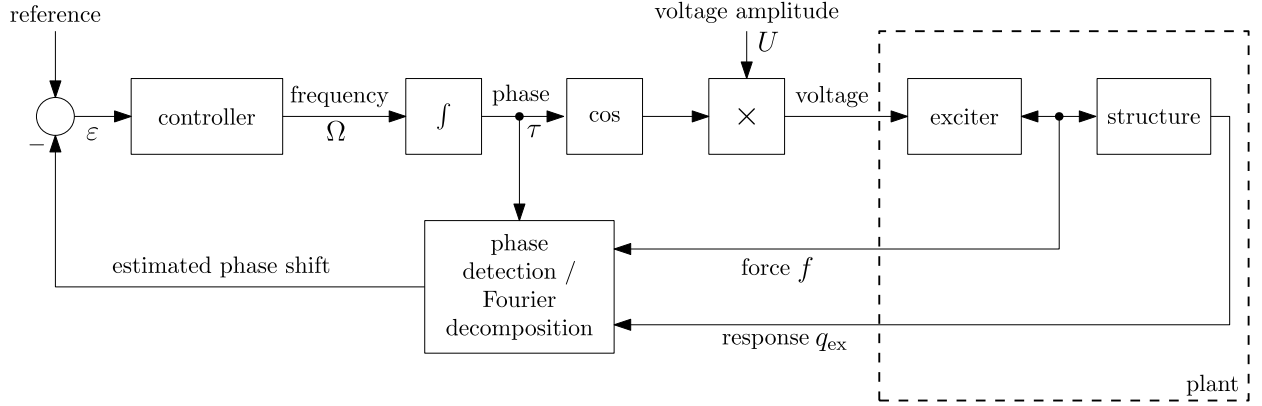


Figure 1: Schematic of considered problem setting.

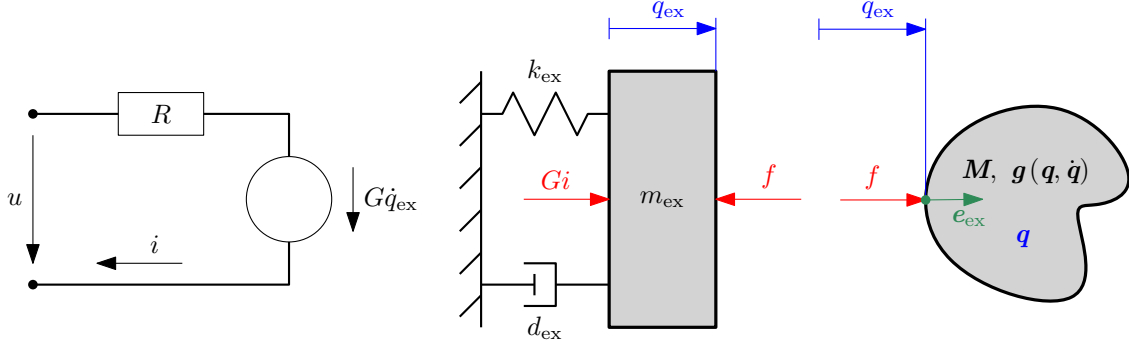


Figure 2: Model of the plant: (left) electrical and (middle) mechanical part of the exciter; (right) structure under test.

2. Problem setting

The problem setting is schematically illustrated in Fig. 1. The closed loop consists mainly of a plant, a phase detector, and a controller. The plant is the union of the structure under test and the vibration exciter. An excitation via a single electro-dynamic shaker with a stinger is considered (Fig. 2), which is the by far most popular setup for nonlinear vibration testing. The transfer of the proposed approach to base excitation seems feasible [7], but is viewed as outside the scope of the present work. The applied force f and the response q_{ex} are measured. As stated above, an adaptive filter is used for phase detection and, more generally, for Fourier decomposition. The difference of the estimated phase lag to the set value (reference) is fed to the controller, which outputs a frequency. Integration of the frequency yields the phase, which is used as argument of a harmonic function that modulates the voltage input to the exciter. In the following, the mathematical model of the closed loop is formulated, fundamental assumptions are specified, and the design parameters to be set by the proposed approach are identified.

In most previous works, a Duffing oscillator was considered as plant model [26, 18]. For wider applicability, a more generic model of the structure under test is considered,

$$M\ddot{\mathbf{q}} + \mathbf{g}(\mathbf{q}, \dot{\mathbf{q}}) = \mathbf{e}_{\text{ex}} f. \quad (1)$$

Herein, $\mathbf{q} \in \mathbb{R}^{n \times 1}$ is the vector of generalized coordinates, where n is the number of degrees of freedom, overdot denotes derivative with respect to time t , $\mathbf{M} = \mathbf{M}^T > \mathbf{0}$, $\mathbf{M} \in \mathbb{R}^{n \times n}$ is the mass matrix, \mathbf{g} are generalized forces, and \mathbf{e}_{ex} describes point and direction of the applied force f . The limiting assumptions on the behavior of the structure are adopted from those underlying the Extended Periodic Motion Concept [5]: $\mathbf{q} = \mathbf{0}$ is an asymptotically stable equilibrium position, and the frequency of the target mode must be

away from any internal resonance condition. This non-resonance condition must hold not only in the linear case, but up to the vibration level of interest. Under those conditions, the structure behaves like a single nonlinear modal oscillator, so that one can achieve phase resonance with a single exciter, and restricting the control to the fundamental harmonic [6, 7]

The goal is commonly to identify the dynamic behavior of the structure under test, not of the plant (which also includes the exciter). To make this distinction, the behavior of the exciter has to be considered. In the present work, the conventional model of an electro-dynamic exciter is used [32, 33],

$$m_{\text{ex}}\ddot{q}_{\text{ex}} + d_{\text{ex}}\dot{q}_{\text{ex}} + k_{\text{ex}}q_{\text{ex}} = Gi - f, \quad (2)$$

$$Ri + G\dot{q}_{\text{ex}} = u, \quad (3)$$

$$q_{\text{ex}} = \mathbf{e}_{\text{ex}}^T \mathbf{q}. \quad (4)$$

It is assumed that the stinger is rigid, so that the shaker armature is regarded as directly attached to the structure at the drive point (Eq. 4). In Eq. 2, m_{ex} is the moving (or dynamic) mass of the exciter. This includes the armature, the coil, possible sensors and the stinger. k_{ex} , d_{ex} denote the mechanical stiffness and damping of the exciter, $G > 0$ is the electromotive force constant, $R > 0$ is the electrical resistance, i is the current, u is the voltage. The self-induction within the electrical part of the exciter is neglected, which is a very common assumption at sufficiently low frequencies. Physically, this means that there is no phase lag between the voltage and the voltage-imposed part of the current (excluding the term $G\dot{q}_{\text{ex}}$ in Eq. 3). The main intentions behind this assumption were to avoid more lengthy expressions in the theoretical derivation, and to avoid having to identify this parameter. In fact, the proposed control design will turn out to require only very few system parameters as input, which are to be obtained based on a conventional shaker-based linear modal analysis, as explained in Appendix A.

The proposed adaptive filter is governed by the set of ordinary differential equations²,

$$\dot{\hat{F}}^{(h)} = 2\omega_{\text{LP}}e^{-ih\tau} \left(f - \Re \left\{ \sum_{h=0}^H e^{ih\tau} \hat{F}^{(h)} \right\} \right) \quad h = 0, \dots, H, \quad (5)$$

$$\dot{\hat{Q}}^{(h)} = 2\omega_{\text{LP}}e^{-ih\tau} \left(q_{\text{ex}} - \Re \left\{ \sum_{h=0}^H e^{ih\tau} \hat{Q}^{(h)} \right\} \right) \quad h = 0, \dots, H. \quad (6)$$

Herein, $\hat{F}^{(h)}$ is the estimate of h -th complex Fourier coefficient of f , and $\hat{Q}^{(h)}$ is the estimate of the h -th complex Fourier coefficient of q_{ex} . At steady state, the truncated Fourier series in the parenthesis of Eq. 5 should be a very good approximation of f , implying $\dot{\hat{F}}^{(h)} \approx \mathbf{0}$. The filter parameters are the order H , and the coefficient $\omega_{\text{LP}} > 0$. The interpretation of ω_{LP} as cutoff frequency of a low pass filter is established in Section 3.1. τ is the integral of the instantaneous frequency Ω (Eq. 8), which, in turn, is the output of the controller (Eq. 9). Thus, Ω is generally time-variable but known, which is in contrast to most applications of adaptive filters, where constant-frequency terms are considered.

²It should be remarked that adaptive filters are more commonly stated in time discrete form; the time-continuous form in Eqs. 5-6 is derived in Appendix B.

The remaining equations of the closed loop system are:

$$u = U \cos \tau, \quad (7)$$

$$\tau = \int_0^t \Omega d\tilde{t}, \quad (8)$$

$$\Omega = \Omega_{\text{ini}} + k_p \varepsilon + k_i I_\varepsilon, \quad (9)$$

$$\varepsilon = \frac{\pi}{2} - \left(\hat{\vartheta}_f - \hat{\vartheta} \right), \quad (10)$$

$$\dot{I}_\varepsilon = \varepsilon, \quad (11)$$

$$\hat{\vartheta}_f = \text{Arg} \left\{ \hat{F}^{(1)} \right\}, \quad (12)$$

$$\hat{\vartheta} = \text{Arg} \left\{ \hat{Q}^{(1)} \right\}. \quad (13)$$

Herein, $U > 0$ is the voltage amplitude. U is prescribed in the present work; the exciter is operated in voltage mode. The addition of an amplitude controller is viewed as a natural extension for future work. A simple proportional-integral phase controller is used in the present work. Compared to a pure integral controller (gain k_i), introducing a proportional term (gain k_p) is known to enable quicker settling. An additional differential term could be used, but it would increase the sensitivity to noise, and it will be shown that noise is the dominant impediment when targeting speed and robustness. I_ε is an auxiliary state variable. ε is the control error. It is defined as the deviation from local phase resonance between fundamental harmonics of forcing and response displacement. If the velocity or the acceleration is measured instead of the displacement, the reference phase $\frac{\pi}{2}$ has to be adjusted accordingly. The control error is obtained from the current estimates, $\hat{\vartheta}_f$ and $\hat{\vartheta}$, of the phase of the force and the response displacement, which are determined from the output of the adaptive filter (Eqs. 12-13).

In summary, for a given plant configuration (structure under test with attached exciter), the parameters of the closed loop are:

- initial frequency: Ω_{ini} ,
- voltage amplitude: U ,
- cutoff frequency and order of adaptive filter: ω_{LP}, H ,
- control gains: k_p, k_i .

The purpose of the present work is to design these parameters to robustly and quickly track the phase resonant backbone curve. Some of the parameters are easier to select than others: The initial frequency Ω_{ini} should simply be near the (linear) modal frequency of the target mode. The voltage amplitude U is stepped to reach different vibration levels. The order of the filter H has to be as high as necessary to capture all relevant harmonics of force and response. Most of the subsequently established theory addresses the selection of the control gains k_p, k_i and the cutoff frequency ω_{LP} , with the goal to robustly and quickly reach a phase-locked state. The theory underlying the proposed approach is described in Section 3. Practical recommendations along with a summary are given in Section 4.

3. Theory behind proposed approach

In this section, the theory behind the proposed approach for robust and quick backbone tracking is established, for the generic plant model (Eqs. 1-4) with the controller defined by Eqs. 5-13. A fundamental assumption is that the amplitude and the phase lag of the plant *evolve slowly* as compared to the *fast oscillation* with frequency Ω , under the action of the phase controller. This implies that Ω changes slowly. The slow-fast decomposition permits to extract the dynamics on the slow time scale using an averaging formalism (Section 3.1), which leads to a set of autonomous first-order ordinary differential equations. The

fixed point of those equations corresponds to the phase-locked state (Section 3.2). The asymptotic behavior around the locked state is then analyzed using linear theory (Section 3.3). By making a few simplifying assumptions (phase-neutral exciter, structure operated in linear regime), the problem becomes amenable to analytical solution. It is shown that the phase transient evolves on the time scale induced by the cutoff frequency of the adaptive filter; i. e., the higher ω_{LP} , the faster the phase locks. The control gains k_p , k_i are selected to optimize the settling of the phase transient.

3.1. Dynamics on slow time scale

The dynamics on the fast time scale, i. e., the oscillation with frequency Ω , is induced by Eqs. 7-8. It will be assumed that $\Omega > 0$. In principle, $\Omega \leq 0$ is possible in the case of very poor initialization, e. g., $\Omega_{ini} < 0$, or in the case of a divergent controller (cf. Eq. 9). Hence, assuming $\Omega > 0$ is not an important restriction in practice. To extract the dynamics on the slow time scale, an averaging formalism is applied. This consists in taking the integral over one period (related to Ω), treating the slowly varying quantities as time-constant. This eliminates the fast time scale τ . Averaging is first applied to the plant in Section 3.1.1, and then to the adaptive filter in Section 3.1.2. The remaining equations of the closed loop system are either algebraic or already in first-order form, so that averaging yields trivial results³.

3.1.1. Plant dynamics on slow time scale

In this section, the model of the structure (Eq. 1) is reduced to a *single nonlinear modal oscillator*. This greatly simplifies the subsequent derivations. In contrast to previous works that analyze the stability of phase-locked loops for vibration testing [25, 26, 18], no restriction to a certain type of nonlinearity is necessary, since the modal properties offer a non-parametric description of rather generic nonlinear terms of arbitrary physical origin. However, the derivation relies on the assumption that such a single-mode reduction is possible. In particular, as stated in Section 2, we assume that the equilibrium position $\mathbf{q} = \mathbf{0}$ is asymptotically stable, and that the target modal frequency is well-separated and not in internal resonance. Under those conditions, a single nonlinear mode dominates the response around the phase-resonant backbone curve. Here, a nonlinear mode is defined according to the Extended Periodic Motion Concept [5], as a family of periodic solutions of $\mathbf{M}\ddot{\mathbf{q}} + \mathbf{g}(\mathbf{q}, \dot{\mathbf{q}}) - 2D\omega\mathbf{M}\dot{\mathbf{q}} = \mathbf{0}$, which continues the target linear mode of the linearized system from $\mathbf{q} = \mathbf{0}$ to finite vibration levels. The artificial negative damping term $2D\omega\mathbf{M}\dot{\mathbf{q}}$ cancels the natural dissipation in period-average. $\omega > 0$ is the fundamental (angular) modal frequency of the periodic oscillation, D is modal damping ratio. The periodic modal oscillation is decomposed into a Fourier series, where the complex Fourier coefficients are expressed as $a\varphi^{(h)}$, and $a > 0$ denotes the modal amplitude. Mass-normalization is used so that $(\varphi^{(1)})^H \mathbf{M} \varphi^{(1)} = 1$, where \square^H denotes the complex conjugate transpose (Hermitian). It should be emphasized that the Fourier coefficients of the modal oscillation are generally complex, allowing for non-trivial phase lags among the material points of the structure under test. The modal properties ω , D , $\varphi^{(h)}$ depend on a , which is not explicitly denoted for brevity. To derive the governing equation of the single nonlinear modal oscillator, the approximation $\mathbf{q} \approx \mathcal{U}(a, \vartheta)$ is made with

$$\mathcal{U}(a, \vartheta) = \Re \left\{ \sum_{h=0}^{\infty} a \varphi^{(h)} e^{ih(\tau + \vartheta)} \right\}. \quad (14)$$

Eq. 14 is substituted into Eq. 1, and it is required that the residual is orthogonal with respect to the fundamental harmonic of the mode. Here, amplitude a and phase lag ϑ are allowed to vary slowly with time, so that averaging can be applied. This way, one obtains [34]

$$2i\Omega \left(\dot{a} + ia\dot{\vartheta} \right) + (-\Omega^2 + 2D\omega i\Omega + \omega^2) a = \varphi^H \mathbf{e}_{ex} F e^{-i\vartheta}. \quad (15)$$

Here and in the following, the abbreviation $\varphi = \varphi^{(1)}$ is used, and similarly $F = F^{(1)}$. Requiring orthogonality only with respect to the fundamental harmonic permits to express the nonlinear term in the projected

³The structure of the equations does not change. Formally, the quantities have to be replaced by their mean values.

equation 15 in closed form, using the amplitude-dependent modal properties. The right-hand side of Eq. 15 is obtained by considering Eqs. 2-7:

$$\varphi^H e_{\text{ex}} F = \frac{\varphi_{\text{ex}} G U}{R} - (-\Omega^2 + 2i\Omega D_{\text{ex}} \omega_{\text{ex}} + \omega_{\text{ex}}^2) \mu_{\text{ex}} a e^{i\vartheta}. \quad (16)$$

Herein, ω_{ex} and D_{ex} are the natural frequency and the damping ratio of the mechanical part of the exciter, where $\omega_{\text{ex}} = \sqrt{k_{\text{ex}}/m_{\text{ex}}}$, and $2D_{\text{ex}}\omega_{\text{ex}} = (d_{\text{ex}} + G^2/R)/m_{\text{ex}}$. Note that the back-electromotive force leads to an apparent viscous damping; i.e., G^2/R is added to the mechanical damping d_{ex} . Further, $\varphi_{\text{ex}} = \varphi^H e_{\text{ex}}$, and $\mu_{\text{ex}} = \varphi_{\text{ex}}^2 m_{\text{ex}}$ denotes the modal mass ratio. For convenience, the phase is normalized in such a way that $\varphi_{\text{ex}} \in \mathbb{R}$ and $\varphi_{\text{ex}} > 0$. This can be done without loss of generality, provided that the shaker is not attached at a vibration node.

3.1.2. Adaptive filter dynamics on slow time scale

By applying averaging to both sides of Eq. 5 and Eq. 6, i.e. taking the integral over one period, one obtains for $h = 1$:

$$\dot{\hat{F}} = \omega_{\text{LP}} (F - \hat{F}), \quad (17)$$

$$\dot{\hat{Q}} = \omega_{\text{LP}} (\varphi_{\text{ex}} a e^{i\vartheta} - \hat{Q}). \quad (18)$$

It is important to note that Eqs. 17-18 are independent of the higher harmonics, thanks to the pairwise orthogonality of the harmonic functions $e^{ih\tau}$ over a period. This also applies to the averaged filter equations corresponding to higher harmonics ($\hat{F}^{(h)}$ with $h \neq 1$ and analogous for $\hat{Q}^{(h)}$); i.e., the averaged filter equations are harmonically decoupled. Further, the interpretation of ω_{LP} is now evident from Eqs. 17-18: In period-average, the adaptive filter acts as first-order low-pass filter with the cutoff frequency ω_{LP} .

The higher ω_{LP} , the faster will the filter reduce the deviation between the Fourier coefficient of the input, F , and the estimate \hat{F} . From the perspective of the slow time scale, thus, $\omega_{\text{LP}} \rightarrow \infty$ seems best. However, higher ω_{LP} lead to more pronounced fluctuation of $\hat{F}^{(1)}$ on the fast time scale, as explained later. Indeed, the dominant constraint for maximizing ω_{LP} is noise. Real noise can have various sources and does not have to be a stationary Gaussian process. In lack of a universally valid noise model, a practical approach for the selection of a suitable ω_{LP} is proposed in Section 4.2.

3.2. Fixed point on slow time scale: the locked state

The dynamics of the closed loop on the slow time scale can be expressed as a system of explicit first-order ordinary differential equations. The state variables are (the period-average of) a , ϑ , \hat{F} , \hat{Q} , and I_ε , which are governed by the ordinary differential equations 15, 17-18, and 11. The equation system is closed by the algebraic equations 9-10, 12-13, and 16.

At the *fixed point*, the state variables are time-constant, which yields the algebraic relations:

$$0 = \varepsilon, \quad (19)$$

$$I_\varepsilon = \frac{\Omega_{\text{ini}} - \Omega}{k_i}, \quad (20)$$

$$0 = \frac{\pi}{2} - (\hat{\vartheta}_f - \hat{\vartheta}), \quad (21)$$

$$\hat{F} = F = |F| e^{i\vartheta_f}, \quad (22)$$

$$\hat{Q} = \varphi_{\text{ex}} a e^{i\vartheta}, \quad (23)$$

$$\hat{\vartheta} = \vartheta, \quad (24)$$

$$\hat{\vartheta}_f = \vartheta_f, \quad (25)$$

$$\Omega = \omega, \quad (26)$$

$$2D\omega^2 a = \varphi_{\text{ex}} |F|. \quad (27)$$

When the control error ε vanishes in period average, the period average of I_ε is constant. It follows that the period-average of Ω is also constant, and equals to the modal frequency, $\Omega = \omega$. This implies that the closed loop has locked onto the phase resonant backbone of the structure under test.

3.3. Design of asymptotic behavior around the locked state

Ideally, the locked state is reached rapidly from arbitrary initial conditions. Global stability analysis would require complete knowledge of the nonlinear system, which is generally not available. Instead, the asymptotic behavior around the locked state will be designed.

As shown in Appendix C, one can reduce the state-space dimension in the linear case. More specifically, one can replace the complex state variables \hat{F} , \hat{Q} by the control error ε . Further, the normalized time $\bar{t} = \omega_{\text{LP}} t$ is introduced, and the state $\bar{I}_\varepsilon = \omega_{\text{LP}} I_\varepsilon$ is used instead of I_ε . Thus, the new state vector is $\mathbf{z} = [a; \vartheta; \varepsilon; \bar{I}_\varepsilon]$ (semicolon denotes vertical concatenation). First-order Taylor series expansion around the fixed point yields a linear autonomous ordinary differential equation system. The corresponding coefficient matrix contains the modal properties and their derivatives with respect to a , evaluated at the fixed point. In the present work, it is proposed to design the control parameters for the low-level regime of the structure under test, and to use these constant parameters throughout the backbone. In addition, a phase-neutral exciter is assumed, which further simplifies the problem, so that an analytical solution can be obtained, enabling a clear understanding of the essential parameter dependencies.

With the above stated simplifications, the system of linear autonomous ordinary differential equations is (Appendix C):

$$\Delta \mathbf{z}' = \mathbf{A}_0 \Delta \mathbf{z}, \quad (28)$$

$$\mathbf{A}_0 = \begin{bmatrix} -\bar{\delta}_p & 0 & -\bar{k}_p \Upsilon & -\bar{k}_i \Upsilon \\ 0 & -\bar{\delta}_p & -\bar{k}_p & -\bar{k}_i \\ 0 & \frac{\delta_p}{\delta_s} & -1 & 0 \\ 0 & 0 & 1 & 0 \end{bmatrix}, \quad (29)$$

where $\Delta \mathbf{z}$ is the deviation from the considered fixed point, $\square' = d\square/d\bar{t}$, and

$$\delta_s = (D\omega)_{\text{lin}}, \quad (30)$$

$$\delta_p = \delta_s + (\mu_{\text{ex}} D_{\text{ex}} \omega_{\text{ex}})_{\text{lin}}, \quad (31)$$

$$\bar{\delta}_p = \frac{\delta_p}{\omega_{\text{LP}}}, \quad (32)$$

$$\bar{k}_p = k_p \frac{(1 + \mu_{\text{ex}})_{\text{lin}}}{\omega_{\text{LP}}}, \quad (33)$$

$$\bar{k}_i = k_i \frac{(1 + \mu_{\text{ex}})_{\text{lin}}}{\omega_{\text{LP}}^2}, \quad (34)$$

$$\Upsilon = \frac{GU}{2R} \left(\frac{\varphi_{\text{ex}}}{(1 + \mu_{\text{ex}})\omega^2} \right)_{\text{lin}}. \quad (35)$$

In the following, positive damping is assumed, of both the structure ($\delta_s > 0$) and the plant ($\delta_p > 0$).

In the first column of \mathbf{A}_0 in Eq. 29, only the first element is nonzero. This means that the evolution of the amplitude does not affect the phase lag, nor the phase control error (or its integral in time). This is an important simplification. One can see that $\mathbf{A}_0(1, 1) = -\bar{\delta}_p$ is an eigenvalue of \mathbf{A}_0 , associated with the *amplitude transient*. Thus, the amplitude transient decays exponentially with $e^{-\bar{\delta}_p \bar{t}}$ in the neighborhood of the locked state. From Eq. 31, it can be found that the damping provided by the exciter actually has a positive effect on the decay of the amplitude transient ($\delta_p > \delta_s$). As discussed below Eq. 16, the exciter damping is composed of a mechanical damping and a back-electromotive force. In the current mode of operation, the exciter amplifier tries to mitigate the back-electromotive force. Thus, for very lightly damped structures, it can be beneficial to operate the exciter amplifier in the *voltage mode* (as presumed throughout this work). It is useful to note that the amplitude transient is governed by the plant, and thus the phase

controller has no influence on it. For very lightly-damped structures, it is likely that the phase settles before the amplitude, especially with the optimized phase transient proposed in this section. Thus, one effectively sweeps along the backbone. If the amplitude transient is deemed too slow, one should extend the feedback loop by a response amplitude controller.

The *phase transient* is determined by the eigenvalues of the lower 3×3 sub-matrix of \mathbf{A}_0 . To have asymptotic stability, all eigenvalues must have negative real part. The quickest decay of the phase transient is expected when the maximum real part among the eigenvalues is minimized. To achieve this, it is useful to note that the trace of this sub-matrix equals the sum of the eigenvalues,

$$\lambda_1 + \lambda_2 + \lambda_3 = -(\bar{\delta}_p + 1) . \quad (36)$$

Since $\Delta \mathbf{z}$ and \mathbf{A}_0 are real, we generally have either three real, or one real and a pair of complex-conjugate eigenvalues. In either case, the sum is real, and $-(\bar{\delta}_p + 1)/3$ is the mean value of the real parts of the eigenvalues. Hence, to minimize the maximum real part among the eigenvalues, λ_1 , λ_2 and λ_3 should all have the same real part

$$\lambda_R = -\frac{\bar{\delta}_p + 1}{3} . \quad (37)$$

With this, the desired eigenvalues can be expressed as

$$\lambda_1 = \lambda_R , \quad (38)$$

$$\lambda_2 = \lambda_R + i\lambda_I , \quad (39)$$

$$\lambda_3 = \lambda_R - i\lambda_I , \quad (40)$$

where $\lambda_I \geq 0$ without loss of generality.

As shown in Appendix C, the above eigenvalue setting can be achieved by selecting the control gains as follows:

$$\bar{k}_p = \frac{\delta_s}{\delta_p} (3\lambda_R^2 + \lambda_I^2 - \bar{\delta}_p) , \quad (41)$$

$$\bar{k}_i = -\frac{\delta_s}{\delta_p} \lambda_R (\lambda_R^2 + \lambda_I^2) . \quad (42)$$

It is easy to see that $\bar{k}_i > 0$ since $\lambda_R < 0$. By substituting λ_R from Eq. 37 into Eq. 41, one can also establish that $\bar{k}_p > 0$ (for the assumed positive damping).

An appropriate value for the imaginary part λ_I still needs to be chosen. It is tempting to simply choose $\lambda_I = 0$, as this should lead to the least-oscillatory phase transient. However, this leads to sub-optimal performance: Indeed, from Eqs. 41-42, one can follow that $\lambda_I = 0$ leads to the smallest control gains, which has the tendency to cause large phase errors during the transient. In the following, a more appropriate choice of λ_I (with $\lambda_I > 0$) is proposed, for the given task of backbone tracking.

Recall that the goal is to track the backbone curve, which is implemented by successive stepping of the voltage amplitude. Suppose that we have reached a steady state, and then increase the excitation level. We thus start from phase resonance ($\varepsilon = 0 = \Delta\varepsilon$, $\Delta\vartheta = 0$), and asymptotically approach this condition afterwards. In the general case, however, the modal frequency will be different, which corresponds to a nonzero initial value for $\Delta\bar{I}_\varepsilon$. In Fig. 3, the solution of the corresponding initial value problem (phase transient) is illustrated for different settings of λ_I . More specifically, the evolution of the (phase) control error, $\Delta\varepsilon$, and the frequency, $\Delta\Omega$, is determined by solving Eq. 28 for the described initial values. Clearly, the higher λ_I , the smaller the maximum control errors, but the larger the frequency overshoots initially. Interestingly, control error and frequency overshoot reach finite limit values for $\lambda_I \rightarrow 0$ and $\lambda_I \rightarrow \infty$, respectively. As a trade-off, we propose to determine λ_I so that maximum control error and maximum frequency overshoot, normalized by their respective limit values, are minimized. While the initial value problem can be solved analytically, this condition leads to a transcendental equation, as shown in Appendix

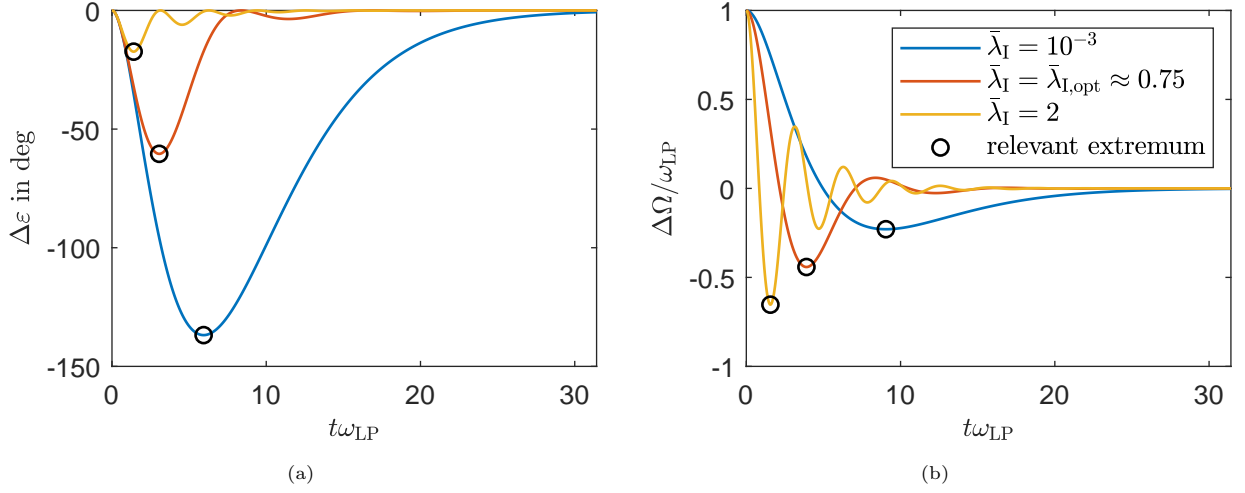


Figure 3: Phase error (a) and frequency shift (b) over time for a unit initial frequency offset. The point labeled *relevant extremum* is used to define the optimal λ_I . $\bar{\delta}_p = 10^{-2}$, $\mu_{ex} = 0$ (implying $\delta_p/\delta_s = 1$).

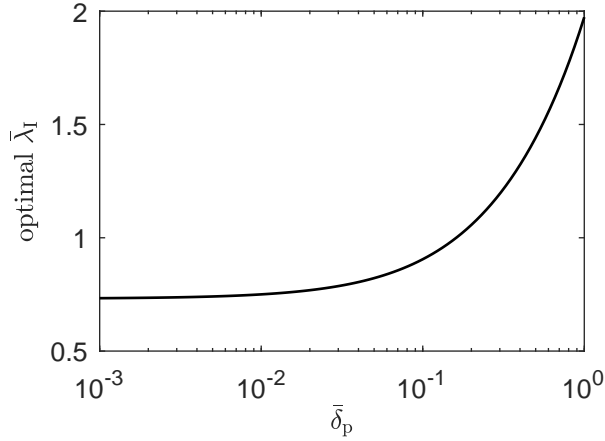


Figure 4: Optimum λ_I leading to the proposed trade-off between control error and frequency overshoot during a step along the backbone. $\bar{\delta}_p$ is the normalized decay rate.

C, which has to be solved numerically. The solution of that equation gives a unique trade-off λ_I for each $\bar{\delta}_p$, as illustrated in Fig. 4. From this figure, one can infer that the higher the plant damping, the higher the proposed λ_I , and, in turn, the higher the control gains. It will later be seen, however, that $\bar{\delta}_p < 10^{-1}$ for reasonably fast adaptive filters and light damping, so that the optimal λ_I does not deviate much from its asymptotic value reached for $\bar{\delta}_p \rightarrow 0$.

4. Practical recommendations and summary of proposed approach

Recall that for a given plant configuration (structure under test with attached exciter), the parameters of the phase resonance test are: initial frequency Ω_{ini} , voltage amplitude U , cutoff frequency ω_{LP} and order H of the adaptive filter, as well as the control gains k_p , k_i . It is proposed to set $\Omega_{ini} = \omega_{lin}$, where ω_{lin} is identified using a conventional linear modal test. The setting of the limits and increments of the voltage amplitude U is discussed in Section 4.1, and it is proposed to increase the voltage along ramps during the backbone tracking. Theoretical considerations on ω_{LP} and H were discussed in Section 3.1.2; a practical, yet

systematic tuning procedure is proposed in Section 4.2. Optimal values for the control gains were derived in Section 3.3. Recommendations on the automatic settling detection and the elimination of hold times are made in Section 4.3 and Section 4.4, respectively. Finally, the overall approach is summarized in an algorithmic form in Section 4.5. As the purpose of backbone tracking is often the identification of the amplitude-dependent modal properties, these are expressed as function of directly acquired quantities in Section 4.6 for completeness.

4.1. Voltage ramps

To track the backbone curve, the vibration level needs to be adjusted. Usually one would like to acquire data also in the almost linear regime, in order to check consistency with results obtained from conventional linear modal testing. A reasonable signal-to-noise ratio is required to obtain a sufficiently robust and fast adaptive filter. This can lead to a lower bound of the vibration level in practice, as discussed below (Section 4.2). The upper bound of the vibration level will be application specific. Examples are the exciter limitations, the intent to avoid structural damage, or the expected vibration level under operating conditions. A sequence of voltage amplitudes $\{U_1, \dots, U_{N_u}\}$ should be specified by the user. The step size should be as small as necessary for the linear theory underlying the control design to hold (i.e., the system remains close to phase resonance / the phase control error remains small). Also, it should be as small as necessary to capture the amplitude-dependence of the quantities of interest with sufficient resolution. On the other hand, the step size should be as large as possible to avoid spurious effort.

The common step-wise (discontinuous) change of U from one specified value to the next could introduce sudden changes in the response. In particular, it could cause higher harmonic and modal distortions. For a smoother transition between voltage levels, half-cosine ramps are proposed,

$$U(t) = U_{i-1} + \frac{1}{2} \left[1 - \cos \left(\frac{2\pi}{T_{\text{ramp}}} (t - t_i) \right) \right] (U_i - U_{i-1}), \quad t_i \leq t \leq t_i + T_{\text{ramp}}, \quad (43)$$

Where for $i = 1$, $U_0 = 0$ is used. It is proposed to set

$$T_{\text{ramp}} = \frac{-\ln(0.05)}{\delta_p} \approx \frac{3}{\delta_p}, \quad (44)$$

which corresponds to the 5% settling time of the amplitude transient (assuming amplitude-constant plant damping).

4.2. Systematic tuning of the adaptive filter

The parameters of the adaptive filter are the order H and the cutoff frequency ω_{LP} . ω_{LP} directly determines the time scale of the phase transient; i.e., if ω_{LP} can be doubled, the test duration can be halved. Thus, ω_{LP} has a very important influence on the speed of the backbone tracking. As explained below, frequency components not considered in the adaptive filter lead to fluctuations of the estimated Fourier coefficients, and, in particular, the estimated phase lag. This may cause considerable distortion of the identified quantities of interest, or impede a (sufficiently) locked state. In the following, the mechanism behind the fluctuations is explained first. Subsequently, the setting of H and ω_{LP} is discussed.

Consider the case of a noise-free, periodic input f that can be described exactly with the selected filter order H . Further, suppose that there is an initial difference between the estimated and the true Fourier coefficients. Then, the filter will enter a transient during which the estimated Fourier coefficients change over time to reduce this difference. During the transient, the multiplication of this difference by the harmonic function generates oscillations in the estimates (cf. Eq. 5). For instance, a deviation for index h_1 generates oscillations with frequency $|h_1 + h|\Omega$ and $|h_1 - h|\Omega$ in the estimated coefficient $\hat{F}^{(h)}$. This holds analogously, both during the transient of the filter and at steady state, when additional frequency components are present, which are not integer multiples of Ω , and thus not contained in the filter. In particular, this applies to distortions in the form of noise. The resulting fluctuations of $\hat{F}^{(h)}$ are larger for larger ω_{LP} . Thus, a higher ω_{LP} leads to a higher sensitivity to noise and larger residual fluctuations at steady state.

The extent of the fluctuations depends also on H . The choice of H is actually easier, as described next, before selecting ω_{LP} .

Even if only the fundamental harmonic is of interest, higher harmonics should be considered in the filter to mitigate the above described spurious fluctuations. Recall that strong modal interactions were assumed to be absent, so that only a moderate contribution of higher harmonics is expected. Still, significant higher harmonics are expected for strong and, in particular, less smooth nonlinearity. Higher harmonics are generally more pronounced when the response is acquired with velocity or even acceleration sensors rather than displacement sensors. The higher H , the lower the risk of spurious fluctuations. On the other hand, the higher H , the higher the computational burden for the real time controller, which may, in turn, limit the maximum achievable sampling rate. In fact, the sampling rate of the acquisition and control system may limit the highest frequency (and thus H) that can be resolved without aliasing. It is proposed to set H as high as possible under those two practical constraints (real time capability, aliasing avoidance).

As explained above, the higher ω_{LP} , the faster the filter, but the stronger the noise-induced phase fluctuations. In other words, faster adaptive filters (higher ω_{LP}) can be used when the signal-to-noise ratio is better. It is a reasonable assumption that noise grows sub-proportionally with the signal, so that the signal-to-noise ratio increases with the vibration level. Consequently, the lowest vibration level of interest dictates the maximum affordable ω_{LP} . To find a suitable value for ω_{LP} , it is proposed to do an open-loop test: The voltage is set to $u = U \cos(\omega_{lin}t)$, where the amplitude U is selected to reach a vibration level in the range of the smallest level of interest along the backbone (typically in the almost linear regime). The phase lag is estimated with a set of adaptive filters (with different ω_{LP}). The adaptive filter with the highest ω_{LP} is selected, which leads to phase fluctuations smaller than a given tolerance. As a tolerance, $\varepsilon_{tol}/2$ is recommended, where ε_{tol} is the tolerance used to define the phase as locked. Based on the authors' experience so far, $\varepsilon_{tol} = 1^\circ$ is recommended; i.e., the phase fluctuations in the open-loop test should remain within $\pm 0.5^\circ$.

Thanks to the open-loop nature of the proposed test, the set of adaptive filters can be run online in parallel, or even applied offline to the acquired excitation and response signals. It is proposed to consider values of ω_{LP} in the range $1/100 < \omega_{LP}/\omega_{lin} < 1$. For larger values, one risks violating the assumption of slow-fast decomposition underlying Section 3⁴. For smaller values, the test duration is likely to become impracticable. If the phase fluctuations are still unacceptable at $\omega_{LP}/\omega_{lin} = 1/100$, one should consider improving the signal-to-noise ratio. This can be achieved by modifying the instrumentation (to reduce noise), and/or to start the backbone tracking at a higher initial vibration level (to increase the signal strength).

4.3. Lock-in detection

To automatically detect that a locked state has been reached, the following algorithm is proposed. The idea is to monitor whether the phase lag is continuously within the specified tolerance, $|\varepsilon| < \varepsilon_{tol}$ for a specified time span. Good results were obtained for a time span of 1-2 linear periods. Additionally, occasional outliers are tolerated, which was found to be useful in the presence of real noise. Such outliers are not expected to significantly distort the final results, since the period average of the output quantities (frequency Ω , Fourier coefficients of response and force) is evaluated in the end, in full accordance with the slow-fast decomposition underlying the theory in Section 3. In practice, a ratio of ten percent outliers led to good results. For an efficient digital implementation, the period-based criterion is converted into a sample-based one. Two counters are used, N_{in} , N_{out} , which are initially set to zero, and updated at every sample. The counter N_{in} is incremented if the estimated phase error is within the specified tolerance, $|\varepsilon| < \varepsilon_{tol}$. If $N_{in} \neq 0$, the counter N_{out} is activated, and it is incremented when $|\varepsilon| > \varepsilon_{tol}$. When N_{out} reaches the maximum number of outliers, both counters are set back to zero. When N_{in} reaches the required number of samples in tolerance, the phase is considered as locked.

⁴There is also a theoretical upper bound $\omega_{LP} < 1/T_s$ with the sampling time T_s , to ensure stability and convergence, which can be derived for harmonic base functions with fundamental frequency Ω using the appendix A in [21]. However, this is believed to be irrelevant in the present context, since $\omega_{LP} \lesssim \Omega \approx \omega_{lin}$ and $\Omega \ll 1/T_s$ to resolve higher harmonics without aliasing.

4.4. Elimination of hold times

In all reported studies of backbone tracking, a sufficiently long section of the steady state was recorded, and a discrete Fourier transform was applied to identify the Fourier coefficients of the acquired (force and response) signals. In contrast, we recommend to directly use the Fourier coefficients estimated by the adaptive filter once the phase has locked. More specifically, the period average is taken, as stated in Section 4.3. In accordance with our experience, the LMS algorithm works sufficiently well that the deviation to the results obtained with the conventional approach (discrete Fourier transform of steady state) is smaller than the repetition-variability inherent to real vibration tests. With the proposed controller design method, the hold times become the most important bottleneck. Thus, by eliminating the hold times, the total test duration can be reduced substantially.

4.5. Summary of the proposed approach

The proposed approach can be summarized in the following algorithm:

- 1: *LINEAR MODAL ANALYSIS*
- 2: Do a shaker-based linear modal analysis.
- 3: For the target mode, obtain ω_{lin} , δ_s as described in Appendix A.
- 4: Estimate moving mass of exciter, m_{ex} , and obtain δ_p , μ_{ex} as described in Appendix A.
- 5: *RANGE TO BE TESTED*
- 6: Specify voltage levels $\{U_1, \dots, U_{N_u}\}$.
- 7: Set T_{ramp} according to Eq. 44.
- 8: *OPEN-LOOP TEST, ADAPTIVE FILTER TUNING*
- 9: Do open-loop test with $u = U_1 \cos(\omega_{\text{lin}} t)$.
- 10: Set ω_{LP} and H as described in Section 4.2.
- 11: *ANALYTICAL DESIGN OF PI CONTROLLER*
- 12: Set $\Omega_{\text{ini}} = \omega_{\text{lin}}$.
- 13: Evaluate $\bar{\delta}_p = \delta_p / \omega_{\text{LP}}$, $\lambda_R = -(\bar{\delta}_p + 1)/3$, and obtain λ_I from Fig. 4.
- 14: Set k_p , k_i according to Eqs. 41-42, Eqs. 33-34.
- 15: *BACKBONE TRACKING*
- 16: **for** $i = 1, \dots, N_u$ **do**
- 17: Apply voltage ramp defined in Eq. 43.
- 18: Wait until phase lock-in detected.

4.6. Amplitude-dependent modal properties

Recall that the assumptions on the structure under test are in line with the Extended Periodic Motion Concept, and nonlinear modal analysis is probably the most important use cases of backbone tracking. Thus, it seems useful to explicitly give the amplitude-dependent modal properties here as function of the acquired data:

$$\omega(a) = \Omega, \quad (45)$$

$$D(a) = \frac{\varphi_{\text{ex}}(a) |F|}{2 \omega^2(a) a}, \quad (46)$$

$$a = \|\Phi_{\text{lin}}^+ \hat{\mathbf{q}}^{(1)}\|, \quad (47)$$

$$\varphi^{(h)}(a) = \frac{1}{a} \hat{\mathbf{q}}^{(h)} \quad h = 0, \dots, H, \quad (48)$$

$$\varphi_{\text{ex}}(a) = \mathbf{e}_{\text{ex}}^T \varphi^{(1)}. \quad (49)$$

In Eq. 47, $\|\square\|$ is the Euclidian norm, and \square^+ denotes the Moore-Penrose pseudo-inverse. The matrix Φ_{lin} contains the mass-normalized linear mode shapes as columns. These can also be obtained by conventional shaker-based linear modal testing. Eqs. 45-46 follow directly from the fixed point established in Section 3.2. Eq. 47 was established in [7]. Eqs. 48-49 have been introduced in Section 3.1.1 and are only repeated here for convenience.

5. Numerical validation of proposed control gain selection

The purpose of this section is to validate the proposed selection of the proportional and integral gains, k_p and k_i , of the controller. Recall that the analytical design relies on linear behavior of the structure under test. A focus is thus placed on the analysis whether this leads to acceptable performance also in the nonlinear regime. In addition, damping is varied in a wide range, which cannot be easily done in a real experiment.

An idealized problem setting is considered (perfect exciter, no noise), where the Duffing oscillator is considered as plant model,

$$\ddot{q} + 2\delta_p \dot{q} + \omega_{\text{lin}}^2 q + \gamma q^3 = F \cos \tau. \quad (50)$$

The parameter γ is set to obtain a 20% frequency shift at unity amplitude.

A harmonic force is directly applied, which corresponds to a perfect exciter. As a consequence, no distinction between plant and structural properties is made, so that $\delta_p/\delta_s = 1$ and $\mu_{\text{ex}} = 0$ are used. As the force is imposed and known, we can set $F \in \mathbb{R}$, $F > 0$, without loss of generality, so that $\vartheta_f = 0$. Consequently, it does not make any sense to apply an adaptive filter to the force; instead, we simply use $\hat{\vartheta}_f = \vartheta_f = 0$.

As the problem setting is noise-free, it is not useful to study the effect of the filter cutoff frequency. $\omega_{\text{LP}}/\omega_{\text{lin}}$ is fixed to 1/10, which equals the value used in the real experiment. A harmonic filter order $H = 9$ is used, which was found sufficiently high to have negligible effect on the depicted results.

Two parameters are varied, the force level F and the damping δ_p . Note that one can eliminate the other parameters in Eq. 50, ω_{lin} and γ , by properly normalizing time and the variable q , respectively. Two scenarios are considered: First, a step is taken from 1% to 2% frequency shift on the backbone. Here ω_{lin} is used as reference. Second, a step is taken from 19% to 20%. The first step is considered to be in the *weakly nonlinear* and the second in the *strongly nonlinear* regime. The force levels F are adjusted accordingly. In either case, the simulation starts from the steady state at the lower excitation level. Steps are preferred here over ramps for simplicity. This seems justified here, since no significant distortion is expected from the discontinuity; in particular, no higher mode can be excited, and the nonlinear term is smooth.

First, the control gains are set as proposed. The results are presented in Fig. 5 for different damping values. For this particular plot, only results for the step from 1% to 2% are shown. The results for the step from 19% to 20% are almost indistinguishable, and not shown for brevity. The depicted damping values $\bar{\delta}_p = \delta_p/\omega_{\text{LP}} \in \{10^{-3}, 10^{-2}, 10^{-1}, 5 \cdot 10^{-1}\}$ correspond to damping ratios $D_{\text{lin}} \in \{0.01\%, 0.1\%, 1\%, 5\%\}$, since $\omega_{\text{LP}}/\omega_{\text{lin}} = 1/10$. It should be stressed that in accordance with the theory presented in Section 3, the time evolution of Fig. 5b-c should be almost constant when plotted against $\bar{t} = \omega_{\text{LP}} t$. Still, it is preferred to use the number of linear periods, $\omega_{\text{lin}} t/(2\pi)$, as time variable, since this is of more technical relevance. Thus, when ω_{LP} is increased by a given factor, the results are expected to be compressed by the same factor on the time axis plotted in Fig. 5.

As expected, the lower the damping, the longer the amplitude transient. In fact, the amplitude does not reach a stationary value for the lowest damping (magenta curve) in the depicted time frame (Fig. 5a). Since the amplitude varies with time, the amplitude-dependent natural frequency also has to vary with time. In general, the settling time is defined as the time it takes until the phase has locked. For this idealized numerical example, no significant phase fluctuations occur, so that the phase is considered as locked simply when $|\varepsilon| < \varepsilon_{\text{tol}} = 0.5^\circ$ for the remaining time. The lower the plant damping, the smaller is the maximum phase error ε . The reason for this is that the amplitude transient is slow, so that the controller can adjust the frequency relatively quickly, which leads to small phase errors. For sufficiently low damping, the phase error always remains within the tolerance, which corresponds to *zero settling time*. Even for higher damping, the maximum phase error does not exceed 1.5° , and the phase locks within less than 20 linear periods or less (blue curve in Fig. 5d). It can generally be observed that once the phase is locked ($|\varepsilon| < \varepsilon_{\text{tol}}$), one obtains an accurate estimate of the amplitude-dependent natural frequency $\omega(a)$ (black dots in Fig. 5c). Here, the reference $\omega(a)$ was obtained from harmonic balance, applied to the Duffing oscillator, evaluated at $a(t)$, the magnitude of the fundamental harmonic estimated by the adaptive filter.

The influence of the control gains on the (phase) settling time is illustrated in Fig. 6. 1200 linear periods were simulated for each parameter set. Near $\bar{k}_i = 0$, and near $\bar{k}_p = 0$ at higher \bar{k}_i , the phase did not lock

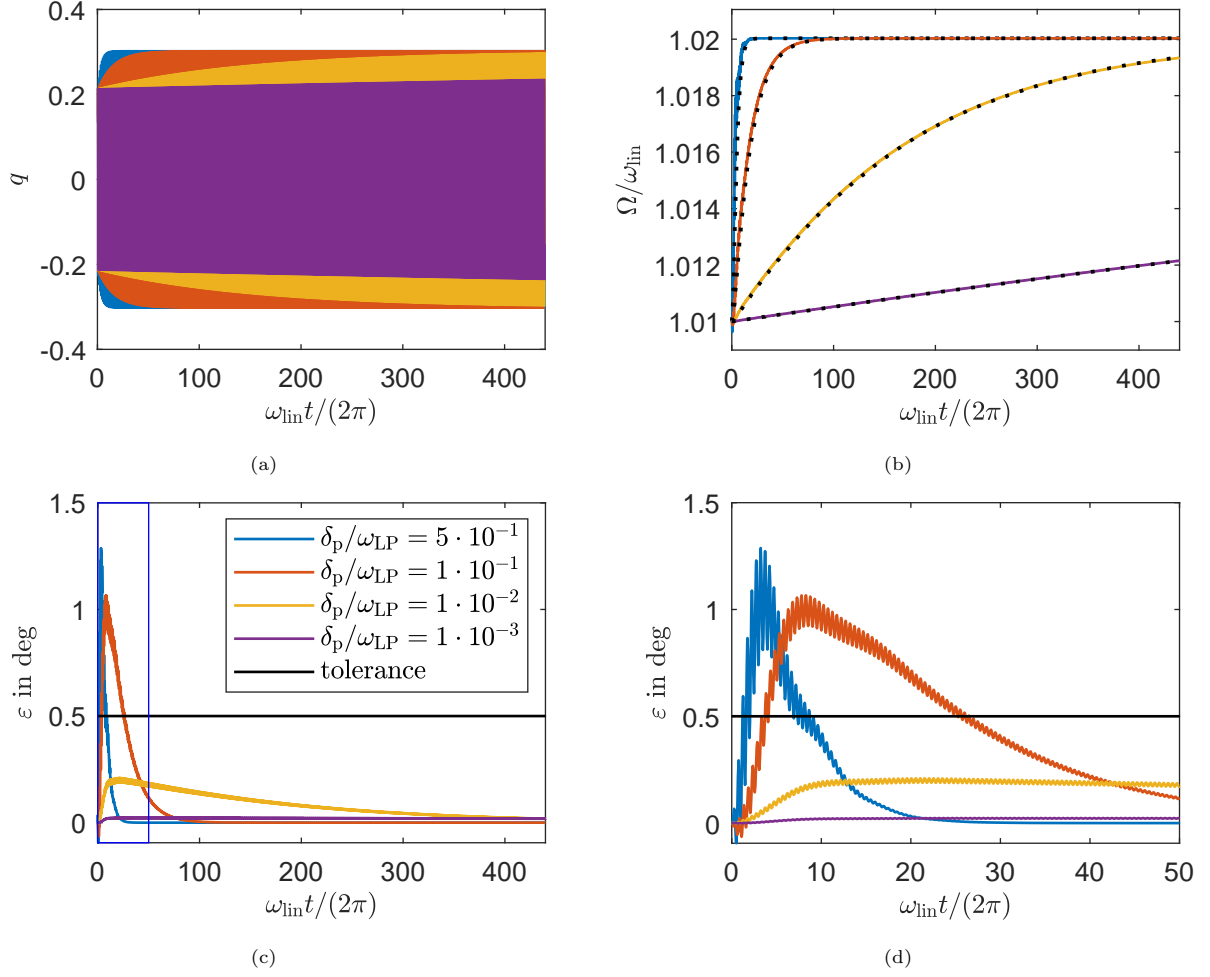


Figure 5: Simulated excitation level step leading to a frequency shift from $1.01\omega_{\text{lin}}$ to $1.02\omega_{\text{lin}}$: time evolution of (a) displacement, (b) excitation frequency, and (c) phase error. (d) is a zoom to the blue box in (c). The legend in (c) applies to all sub-figures. The black dots in (b) depict the natural frequency $\omega(a(t))/\omega_{\text{lin}}$ computed based on harmonic balance using the instantaneous amplitude estimated by the adaptive filter. Control gains k_i, k_p were chosen according to the proposed design procedure for each damping value. As time variable, the number of linear periods is used, $\omega_{\text{lin}} t / (2\pi)$. $\omega_{\text{LP}}/\omega_{\text{lin}} = 0.1$.

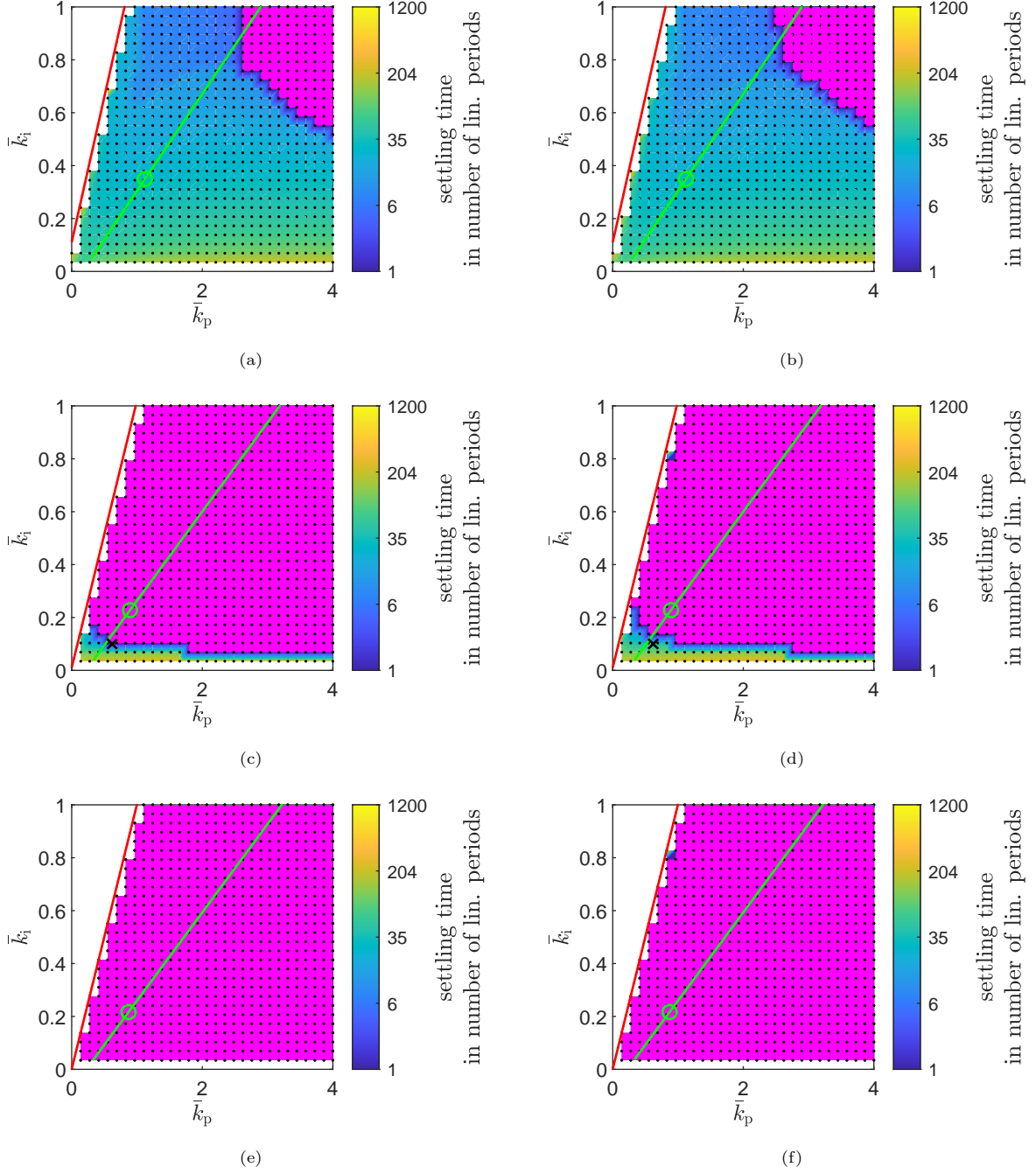


Figure 6: Controller settling time (color scale) as function of control gains \bar{k}_p , \bar{k}_i . The excitation level step leads to a frequency shift from $1.01\omega_{lin}$ to $1.02\omega_{lin}$ (left column), or from $1.19\omega_{lin}$ to $1.20\omega_{lin}$ (right column). The damping is set as $\delta_p = 10^{-1}$ (top), $\delta_p = 10^{-2}$ (middle), $\delta_p = 10^{-3}$ (bottom). As time variable, the number of linear periods is used, $\omega_{lin}t/(2\pi)$. $\omega_{LP}/\omega_{lin} = 0.1$. Line corresponding to three eigenvalues with equal real parts (—), proposed design point (○), stability limit (—), region with zero settling time (■). Where the plot is blank (white), the phase did not settle within the simulated time of 1200 linear periods. The black crosses (×) in the middle row indicate the design point implemented in the real experiment as explained in Section 6.

within the simulated time span. This could either mean divergence or a finite settling time exceeding 1200 linear periods. A closer inspection shows that near $\bar{k}_i = 0$, the closed loop does not diverge; still, steady-state control error exceeds the tolerance. On the other hand, divergence occurs near $\bar{k}_p = 0$ for higher \bar{k}_i . A stability limit can be predicted based on the results of Section 3: All eigenvalues of the lower 3×3 sub-matrix of \mathbf{A}_0 in Eq. 29 have negative real part for $\delta_p, \delta_s > 0$, $k_i, k_p > 0$, under the condition

$$\bar{k}_i < (\bar{\delta}_p + 1)(\bar{\delta}_p + \bar{k}_p), \quad (51)$$

which can be derived using the Routh–Hurwitz criterion [35]. The corresponding stability limit is also depicted in Fig. 6. It is in very good agreement with the numerical simulation results, for both excitation levels. Clearly, a proportional gain is needed to achieve stability for higher \bar{k}_i and reasonable settling times. The line corresponding to $\bar{k}_p(\lambda_I), \bar{k}_i(\lambda_I)$ according to Eqs. 41-42 is depicted in Fig. 6 as green line. The line departs at $\bar{k}_p, \bar{k}_i > 0$ for $\lambda_I = 0$ in the bottom left of the diagrams. As theoretically reasoned in Section 3, $\lambda_I = 0$ leads to relatively poor performance. The proposed setting of λ_I according to Fig. 4 (represented in Fig. 6 by a circular marker), in contrast, leads to very good performance for all considered damping values, both in the weakly and in the strongly nonlinear regime. Remarkably, the results obtained for the weakly and the strongly nonlinear case are very similar. This supports the proposed design based on the linear behavior of the structure. Apparently, the settling time depends only weakly on the precise value of the controller parameters near the proposed optimum. In this sense, the proposed design can be regarded as robust. Zero settling time is reached for higher control gains. In full accordance with the observations made in Fig. 5, the region of zero settling time increases for decreasing damping (from top to bottom in Fig. 6). For higher damping, the proposed design does not lead to zero settling time. For the idealized problem setting (no noise, perfect exciter, single-degree-of-freedom oscillator), higher gains could be used to reach zero settling time even for larger damping. In a real experiment, however, it is expected that this amplifies noise, and leads to less robust behavior.

6. Experimental assessment of proposed approach

The purpose of the present section is to assess the performance of the proposed approach in a real experiment. Compared to the virtual experiment in Section 5, this permits, in particular, to analyze the robustness to real noise, and possible deviations of the structure under test or the exciter from the behavior assumed in Section 3.

6.1. Test rig

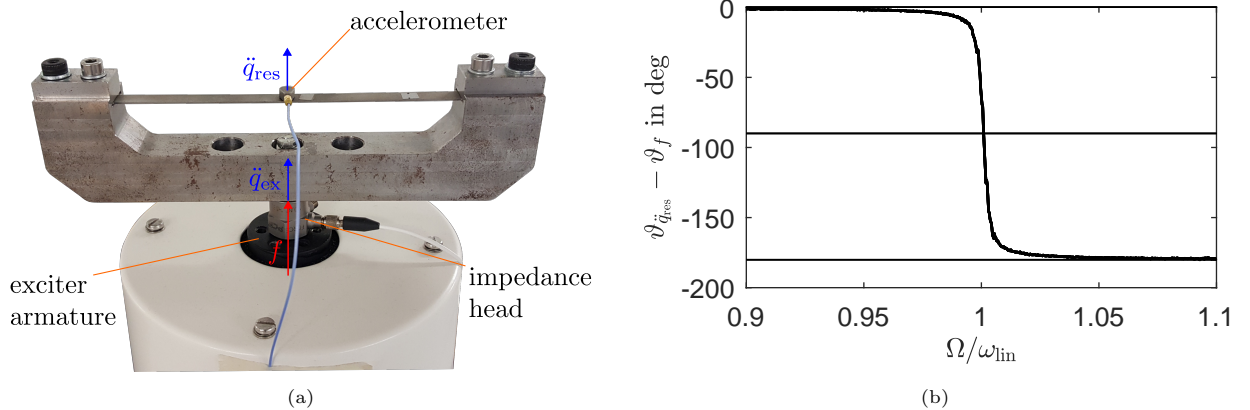


Figure 7: Test setup: (a) test rig consisting of a thin beam clamped at both ends via bolted joints to a stiff frame, mounted on the armature of an electro-dynamic exciter and (b) phase response in the linear regime vs. excitation frequency.

The structure under test consists of a thin, straight beam, clamped to a stiff frame (Fig. 7a). The beam has a free length of 140 mm, a thickness of 0.8 mm, and a width of 8 mm. Since the beam is clamped at both ends, axial movement is constrained, so that bending deformation induces membrane stretching, increasing the bending stiffness (nonlinear bending-stretching coupling). In the considered amplitude range, this led to ca. 20% frequency shift of the fundamental bending mode.

The frame was mounted onto the armature of a vibration exciter (DataPhysics SignalForce V20). The exciter amplifier (DataPhysics SignalForce PA100E) was operated in voltage mode. The excitation force was measured via an impedance head (PCB 288D01). If the purpose of the backbone tracking is to obtain the amplitude-dependent modal properties in accordance with the Extended Periodic Motion Concept, applied force and drive point response should be in (local) phase resonance [6, 7]. For the given setup, thus, one should require phase resonance between the acceleration signal \ddot{q}_{ex} and the force signal f of the impedance head (Fig. 7a). However, due to the relatively low sensitivity of the impedance head, the acceleration signal had a very poor signal-to-noise ratio, so that it was decided not to use this signal. Instead, the response signal \ddot{q}_{res} acquired by the acceleration sensor (PCB 352A21) placed at the beam's center was used, which led to an acceptable signal-to-noise ratio. Phase resonance was required between this response signal and the force measured with the impedance head, as explained in Section 6.2.

The above described test rig has been used in multiple studies, among others in [7, 36, 15]. In particular, the amplitude-dependent modal properties identified using phase-resonance testing have been successfully validated via frequency-response measurements [7] and via Control-Based Continuation [15]. Also, those amplitude-dependent modal properties have been used to update and validate an analytical model of the doubly clamped beam [36]. The focus of the present section is placed on the assessment of the speed and robustness of the proposed approach for backbone tracking, and its comparison to the validated state of the art.

6.2. Linear modal analysis

Table 1: Results of the linear modal analysis. ω_{lin} and D_{lin} are the linear modal frequency and damping ratio of the structure under test, respectively. $\tilde{\omega}_{\text{lin}}$ and \tilde{D}_{lin} are the corresponding values of the plant (including the exciter).

Quantity	Mean Value	Standard Deviation
$\omega_{\text{lin}}/(2\pi)$	175.5 Hz	0.5 Hz
D_{lin}	1.6×10^{-3}	2.0×10^{-4}
$\tilde{\omega}_{\text{lin}}/(2\pi)$	175.6 Hz	0.8 Hz
\tilde{D}_{lin}	1.8×10^{-3}	3.0×10^{-4}

A shaker-based linear modal analysis was carried out. To this end, a pseudo-random voltage of relatively low level was generated and fed to the shaker amplifier (nominal voltage level 10 mV). With the specified maximum frequency of 312.5 Hz, frequency resolution of 4.9 mHz, and 8 windows with 50% overlap, the total measurement duration was about 90 s. The frequency response functions from voltage to response and from force to response were estimated using the common H1 estimator. As the considered mode is well-separated and damping is light, the linear natural frequencies and damping ratios were identified using the simple peak picking (single-degree-of-freedom) method. Several repetitions were done, before after and between nonlinear tests, leading to a total of 21 values. The intent behind these repetitions was to monitor any changes over time e. g. due to thermal sensitivity, settling or wear in the frictional clamping. Mean and standard deviation of the modal properties were determined, and are listed in Table 1. The rather small standard deviations indicate that the system is in very good approximation time-invariant.

Because the response could not be measured at the drive point (as explained in Section 6.1), φ_{ex} and, thus, μ_{ex} could not be determined. Instead, the linear modal frequency $\tilde{\omega}_{\text{lin}}$ and damping ratio \tilde{D}_{lin} of the plant are given, where $\tilde{\delta} = \tilde{D}_{\text{lin}}\tilde{\omega}_{\text{lin}}$, in accordance with Eq. A.3. Apparently, the values of the plant are almost the same as those of the structure under test, suggesting $\mu_{\text{ex}} \ll 1$.

As stated in Section 6.1, the response was not measured at the drive point but at a point on the beam (Fig. 7a). Consequently, one has to revisit the phase resonance condition. Analogous to Eq. 4, we define

a response coordinate $q_{\text{res}} = \mathbf{e}_{\text{res}}^T \mathbf{q}$, where $\mathbf{e}_{\text{res}} \in \mathbb{R}^{n \times 1}$ describes point and direction of the response. In accordance with the assumption that the target mode is away from any internal resonance condition, the structure behaves like a single nonlinear modal oscillator (see Section 2). In particular, the fundamental Fourier coefficient of the response coordinate is $Q_{\text{res}}^{(1)} = \mathbf{e}_{\text{res}}^T \boldsymbol{\varphi} a e^{i\vartheta}$ (Section 3.1.1). Recalling that $a > 0$, the response phase is thus $\vartheta_{\text{res}} = \text{Arg}\{\mathbf{e}_{\text{res}}^T \boldsymbol{\varphi}\} + \vartheta$. Herein, ϑ is the phase at the drive point since $\mathbf{e}_{\text{ex}}^T \boldsymbol{\varphi} = \varphi_{\text{ex}} > 0$ was used for normalizing the modal phase (Section 3.1.1). Under the assumption of light damping (in addition to the no-internal-resonance condition), all material points move phase-synchronously in the modal oscillation; i. e., $\boldsymbol{\varphi} \in \mathbb{R}^{n \times 1}$. Thus, $\mathbf{e}_{\text{res}}^T \boldsymbol{\varphi} \in \mathbb{R}$, so that $\text{Arg}\{\mathbf{e}_{\text{res}}^T \boldsymbol{\varphi}\}$ can only assume two values, either 0 or $-\pi$. In fact, $\text{Arg}\{\mathbf{e}_{\text{res}}^T \boldsymbol{\varphi}\} = -\pi$ can be followed from the phase of the frequency response function from f to \ddot{q}_{res} . This phase, $\vartheta_{\ddot{q}_{\text{res}}} - \vartheta_f$, is depicted as function of the frequency Ω in Fig. 7b; it was also obtained from the above described linear test. Note that the fundamental harmonic phase of acceleration and coordinate are related by $\vartheta_{\ddot{q}_{\text{res}}} = \vartheta_{q_{\text{res}}} + \pi$. With this, we obtain $\vartheta_{\ddot{q}_{\text{res}}} - \vartheta_f = \vartheta - \vartheta_f + \pi + \text{Arg}\{\mathbf{e}_{\text{res}}^T \boldsymbol{\varphi}\}$. From Eq. 15, we obtain $\vartheta - \vartheta_f = -\text{Arg}\{-\Omega^2 + 2D\omega i\Omega + \omega^2\}$ at steady state ($\dot{a} = 0 = \dot{\vartheta}$), which starts near 0 before resonance ($\Omega < \omega$), goes through $-\pi/2$ at resonance ($\Omega = \omega$), and then approaches $-\pi$ beyond resonance ($\Omega > \omega$). This matches precisely the evolution of $\vartheta_{\ddot{q}_{\text{res}}} - \vartheta_f$ depicted in Fig. 7b. It is thus concluded that $\text{Arg}\{\mathbf{e}_{\text{res}}^T \boldsymbol{\varphi}\} = -\pi$. With this, we are able to reformulate the phase error defined in Eq. 10,

$$\varepsilon = \frac{\pi}{2} + \hat{\vartheta} - \hat{\vartheta}_f = \frac{\pi}{2} + \hat{\vartheta}_{\ddot{q}_{\text{res}}} - \hat{\vartheta}_f, \quad (52)$$

using the phases of the measured quantities, force f , acceleration \ddot{q}_{res} , which are estimated by the adaptive filter.

6.3. Open-loop test, adaptive filter tuning

A dSPACE MicroLabBox was used to implement the backbone tracking, including the phase-locked loop and signal acquisition. A sampling frequency of 10 kHz was used, which leads to ca. 50 samples per period of the target mode. As proposed in Section 4.5, an open-loop test was carried out first, where $u = U \cos(\omega_{\text{lin}} t)$ is fed to the shaker amplifier. Two voltage amplitudes U were specified, namely 5 mV, which corresponds to the almost linear regime of the structure under test, and 70 mV, which is far in the nonlinear regime (leading to about 20% natural frequency shift). Force f and acceleration \ddot{q}_{res} were recorded; a representative steady-state time series is shown in Fig. 8. As expected, the signal-to-noise ratio is much better at the higher voltage level.

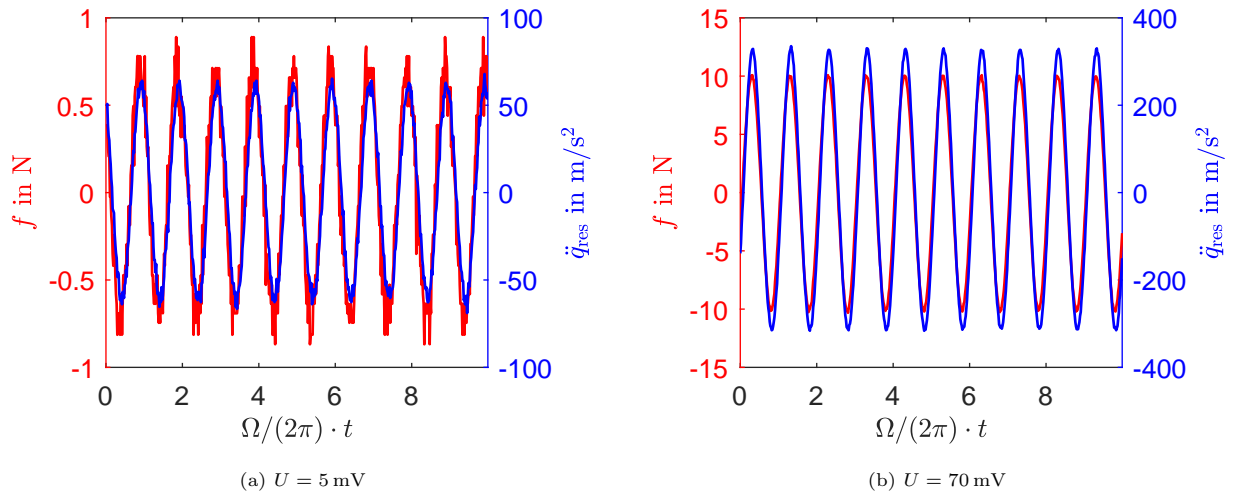


Figure 8: Open-loop test: representative steady-state section of acquired force and response signal. $\Omega = \omega_{\text{lin}}$.

One may notice that f and \ddot{q}_{res} are almost in phase leading to $\varepsilon \lesssim \pi/2$ (see Eq. 52). This may seem

surprising at first sight, given that at phase resonance $\varepsilon = 0$ has to hold. However, $\varepsilon = 0$ is only ensured in the closed-loop test. For the given lightly damped system, the phase is highly sensitive to the frequency near resonance (Fig. 7b). Apparently, the actual natural frequency is slightly higher than the ω_{lin} specified in the open-loop test. From Fig. 7b, one can infer that if the excitation frequency is only one percent below the natural frequency, f and \ddot{q}_{res} are almost in phase ($\vartheta_{\ddot{q}_{\text{res}}} - \vartheta_f \lesssim 0$). At the higher voltage level, the actual modal frequency is higher, so that $\vartheta_{\ddot{q}_{\text{res}}} - \vartheta_f$ is even closer to zero, and thus ε is close to $\frac{\pi}{2}$. Next, the harmonic order H of adaptive filter is selected. Then, the effect of cutoff frequency ω_{LP} is analyzed, and the results are compared to conventional synchronous demodulation (used in most implementations of phase-locked loops in the context of vibration testing, see e.g. [18, 13]).

6.3.1. Selection of harmonic order H

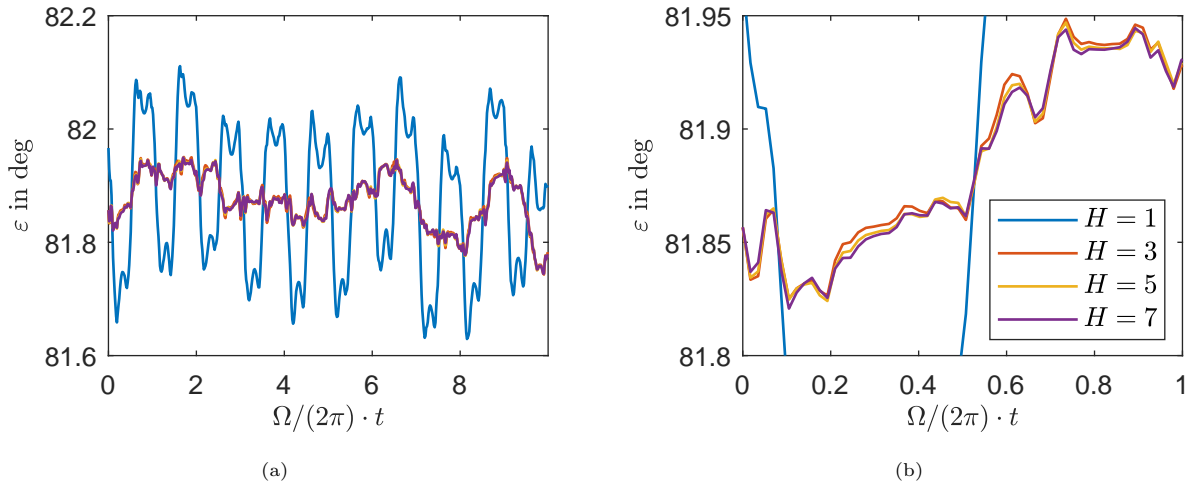


Figure 9: Open-loop test: Phase error estimated by adaptive filter for different harmonic orders H , at the high voltage level $U = 70 \text{ mV}$. $\Omega = \omega_{\text{lin}}$, $\omega_{\text{LP}}/\omega_{\text{lin}} = 1/10$. (b) is zoom of (a).

The effect of harmonic order H was studied only at high vibration level, where more pronounced higher harmonics are expected. Starting from zero initial conditions, $\hat{Q}^{(h)} = 0 = \hat{F}^{(h)}$ for all $h = 0, \dots, H$, the adaptive filter was applied to a sufficiently long time section, to ensure that the depicted results are independent of the initial conditions. The results shown in Fig. 9, which correspond to the time span shown in Fig. 8b.

Considerable fluctuations occur when the filter does not account for the higher harmonics present in the signal ($H = 1$). Adding the third harmonic ($H = 3$) substantially reduces those fluctuations. $H = 7$ was used throughout the present work.

6.3.2. Selection of cutoff frequency ω_{LP} , comparison to synchronous demodulation

In Fig. 10, the effect of the cutoff frequency ω_{LP} is illustrated, both at low (left column) and at high (right column) voltage level. The phase lag estimated by the adaptive filter is compared to that obtained with conventional synchronous demodulation in each sub-figure. A drift is visible at low voltage level (Fig. 10 left column), which is attributed to thermal effects: When the temperature increases during the vibration test, the natural frequency varies slowly with time. This is the case even in the considered open-loop test at a fixed frequency. The phase lag varies accordingly.

It is very clear from the depicted results that the adaptive filter is superior to synchronous demodulation in all cases (each sub-figure of Fig. 10). More specifically, for the same cutoff frequency and input signal, the adaptive filter leads to smaller fluctuations in the estimated phase lag. Further, the fluctuations in the output of the adaptive filter seem to be erratic, which suggests that all relevant frequency components of the signal have been captured and the remaining fluctuations are due to random noise. In contrast, the

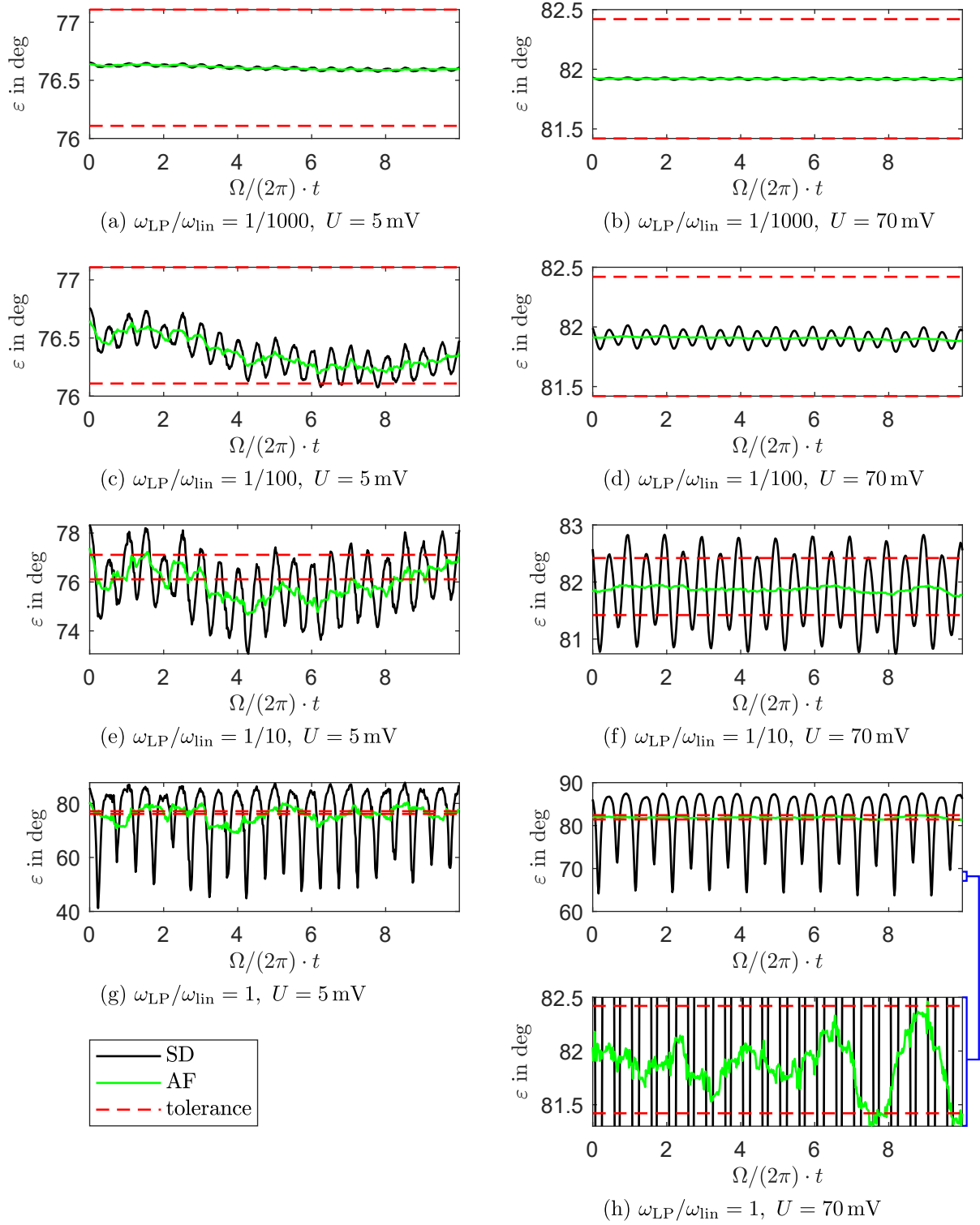


Figure 10: Open-loop test: Phase error estimated by adaptive filter (AF) and synchronous demodulation (SD) for different cutoff frequencies ω_{LP} (increasing from top to bottom row), at low (left) and high (right) voltage level. $\Omega = \omega_{lin}$. Tolerance ($\varepsilon_{tol} = 0.5^\circ$) is defined around the mean value of ε obtained from the adaptive filter. The legend (bottom, left) is valid for all panels.

output of synchronous demodulation shows a periodic distortion with twice the excitation frequency, which can be best seen for lower cutoff frequencies (rows 1-3 in Fig. 10). This is inherent to the signal mixing within synchronous demodulation, where $\cos \tau$ and $\sin \tau$ are multiplied with the input signal. This periodic distortion can only be reduced, but not eliminated, by decreasing the cutoff frequency of the low pass filter (i.e. going from bottom to top row in Fig. 10).

A threshold of $\varepsilon_{\text{tol}}/2 = 0.5^\circ$ was proposed in Section 4.2 for acceptable fluctuations of the estimated phase lag. As explained above, the phase error ε is far from zero in the open-loop test. Hence, fluctuations are deemed acceptable if $|\varepsilon - \varepsilon^*| \leq \pm 0.5^\circ$, where ε^* is the mean value of ε . This tolerance band is indicated via dashed red lines in Fig. 10. In the closed-loop test, of course, $|\varepsilon| < \varepsilon_{\text{tol}} = 1^\circ$ was ensured. For $U = 5 \text{ mV}$, the phase fluctuations remain within the tolerance for an adaptive filter with $\omega_{\text{LP}}/\omega_{\text{lin}} = 1/100$ (Fig. 10c), but not with $\omega_{\text{LP}}/\omega_{\text{lin}} = 1/10$ (Fig. 10e). For $U = 70 \text{ mV}$, an adaptive filter with $\omega_{\text{LP}}/\omega_{\text{lin}} = 1/10$ is sufficient (Fig. 10f), but not with $\omega_{\text{LP}}/\omega_{\text{lin}} = 1$ (Fig. 10h). Thus, as explained in Section 4.2, a higher cutoff frequency can be used when the signal-to-noise ratio is higher. For backbone tracking, the lowest voltage level was set to $U_1 = 10 \text{ mV}$, and an adaptive filter with $\omega_{\text{LP}}/\omega_{\text{lin}} = 1/10$ was used, which performed well throughout the considered voltage range. Going to lower voltage levels would have required a lower cutoff frequency (or an instrumentation that reduces the noise level).

6.4. Backbone tracking

15 voltage levels were specified in the range from $U_1 = 10 \text{ mV}$ to $U_{15} = 70 \text{ mV}$. The first four steps were set to be smaller than the remaining equidistant ones, in order to improve the resolution at lower amplitudes. Using the 5% amplitude settling time proposed in Section 4 would have led to a ramp duration of about 250 linear periods, for the very light damping of the plant (cf. Table 1). To test the robustness of the proposed method, it was decided to use 100 linear periods as ramp duration only, which corresponds to a 30% amplitude settling time.

The test rig was analyzed previously using synchronous demodulation and a heuristically tuned controller [7, 36, 15]. Those heuristic designs serve as reference for the systematic design obtained with the proposed approach. The controller used in [36, 15] contained also a differential term (gain k_d), for which Eq. 9 would have to be replaced by $\Omega = \Omega_{\text{ini}} + k_d \dot{\varepsilon} + k_p \varepsilon + k_i I_\varepsilon$. The cutoff frequency and the control gains are specified in Table 2.

For the given adaptive filter and plant damping, we have $\bar{\delta}_p = \delta_p/\omega_{\text{LP}} \approx \tilde{D}_{\text{lin}}\omega_{\text{lin}}/\omega_{\text{LP}} = 10\tilde{D}_{\text{lin}} \approx 0.02$. This leads to $\lambda_R = -0.34$ (Eq. 37), $\lambda_I \approx 0.8$ (Fig. 4), and finally to the proposed design values $\bar{k}_p = 0.97$, $\bar{k}_i = 0.26$ (Eqs. 41-42). In the actual experiment, slightly smaller gains $\bar{k}_p = 0.62$, $\bar{k}_i = 0.10$ were implemented, denoted as *Systematic* design in Table 2. There was no intention to deviate from the proposed design; the discrepancy was noted long after the tests were completed. The performance for the proposed design is expected to be slightly better than the implemented one: For the given $\bar{\delta}_p$, the results in Fig. 6(middle row) should be representative. In those two sub-figures, the proposed design is indicated as green circle, and the implemented design as black cross. Because of the rather low sensitivity of the settling time in that range (Fig. 6 middle row), but the difference between proposed and implemented design is not expected to be significant.

For each phase-locked loop design in Table 2, the backbone was tracked upwards and downwards, and two times in a row; i.e., four backbones are obtained for each controller design. The results are depicted in Fig. 11a. A small but deterministic difference can be identified between upward and downward stepping. This is in agreement with previous works [36, 15], and is attributed to the same cause as the drift observed in the open-loop test (Fig. 10): thermal effects. In particular, when the beam heats up during the test, the axial prestress varies, which leads to slightly different linear and nonlinear behavior. In spite of this, the tests are well-repeatable, and no significant difference of variability can be identified among the individual control designs. Consequently, the remaining deviations are attributed to the (small but inevitable) repetition-variability inherent to the test rig. Hence, it is concluded that all control designs provide consistent backbones.

To compare the experimentally obtained backbones to a ground truth, the result of the analytical model from [36] is also shown in Fig. 11a. The analytical model relies on the von Karman beam theory, and takes the form of a modal model, truncated to the five lowest-frequency bending modes. The finite rotational

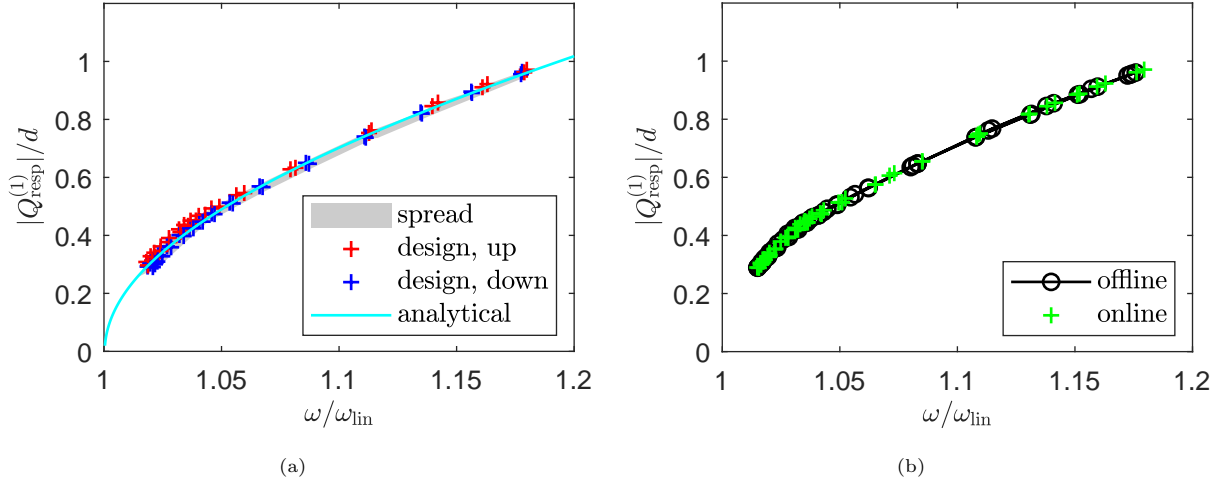


Figure 11: Backbone tracking results: (a) exemplary run with the *Systematic* design (voltage successively increasing (+), decreasing (+)) compared with the spread obtained from all backbone tests (■) and the result obtained with the analytical beam model (—); (b) *offline* evaluation of hold times using discrete Fourier transform vs. *online* estimation using adaptive filter. $|Q_{\text{resp}}^{(1)}|/d$ is the fundamental harmonic of the response displacement at the beam’s center, estimated by the adaptive filter, divided by the beam’s thickness.

stiffness identified in [36] was directly adopted. The different thickness and width of the beam used in the present work were accounted for. Further, the mass of the acceleration sensor was taken from the data sheet (0.6 g), the dynamic mass of the cable and the connector was estimated (0.77 g), and their combined effect was considered in the model. To account for the slightly higher tightening torque, a higher axial clamping stiffness was used (33 N/ μm instead of 19 N/ μm). Thanks to the excellent agreement with the analytical model, the experimentally obtained backbones are regarded as valid.

Table 2: Performance of phase-locked loop designs for backbone tracking. AF denotes adaptive filter and SD synchronous demodulation.

Parameter set	Phase detector	$\omega_{\text{LP}}/\omega_{\text{lin}}$	k_p in s^{-1}	k_i in s^{-2}	k_d	settling time in lin. periods
Systematic	AF, $H = 7$	0.1	68.47	1248	0	120
Heuristic 1 [15]	SD	0.002	150	50	40	1150
Heuristic 2 [36]	SD	0.002	200	100	10	680
Mixed	AF, $H = 7$	0.1	200	100	10	620

As the different phase-locked loop designs provide consistent and valid results, it is fair to compare their efficiency in terms of settling time. To detect phase settling, $N_{\text{in}} = 100$ consecutive samples (approx. 1.8 linear periods) were required to fall below the threshold $|\varepsilon| \leq \pm 0.5^\circ$, with a 10% outlier tolerance (cf. Section 4.3). The lock-in detection in each step was started after completing the defined ramp duration. Hence, the minimum possible settling time is 101.8 linear periods. The mean settling time, taken over all acquired backbone points is listed in the right column of Table 2. The settling time for the individual voltage levels, taken as mean of the respective four backbone points at the same voltage level, is given in Fig. 12. The systematic design leads to a phase lock, in average, only slightly higher than the minimum of 101.8 linear periods. Thus, the ramp is the bottleneck and could probably be further shortened. In addition to the short average value, it is noteworthy that the settling time varies only slightly from voltage level to voltage level. In contrast, the heuristic designs perform much worse, with a 5 – 10 times longer settling time, and a much larger variation of the settling time from voltage level to voltage level. The *Mixed* design, with the parameters listed in the last row of Table 2, combines the heuristic control gains from the *Heuristic 2* design [36] with the proposed adaptive filter. The settling times are very similar to the *Heuristic 2* design. This

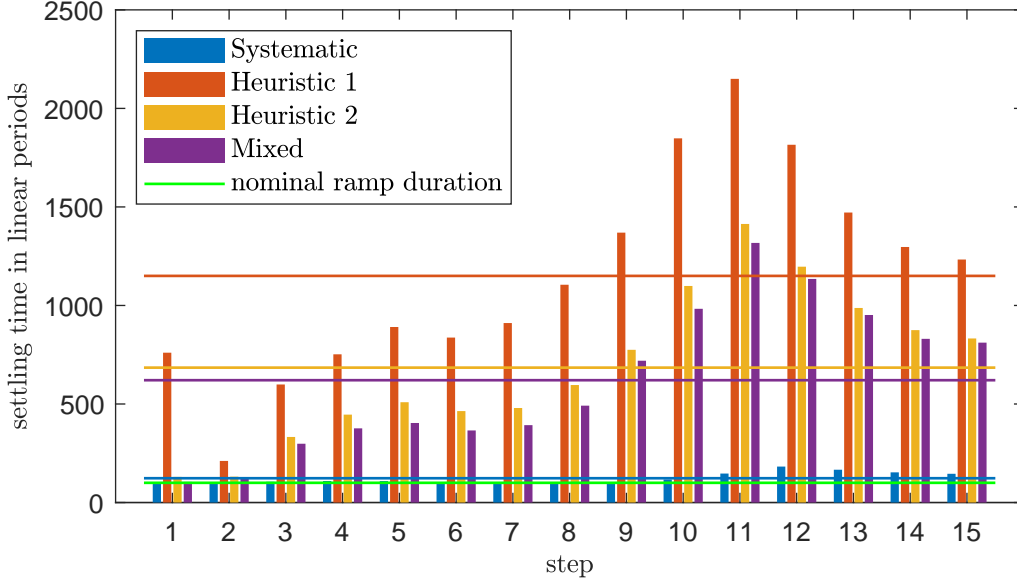


Figure 12: Settling time for each backbone point depending on the phase-locked loop design. The horizontal lines indicate the mean over all steps.

implies that the speed and the robustness achieved with the proposed design approach are not only due to the adaptive filter, but also due to the design of the control gains.

It must be emphasized that the durations of the finally carried out backbone tests may give rise to an incomplete picture, since the preparation effort is missing. In particular, the heuristic designs were obtained as the result of trying a large number of different, manually specified parameter combinations (k_p , k_i , k_d). The duration of this trial and error phase can take anything from minutes to hours. In contrast, the proposed design method does not require such a trial and error phase. On the other hand, the preparation of the proposed design method requires a linear modal test and an open-loop sine test. The open-loop sine test can be very short, e.g., 100 periods (less than 1 s). The linear modal test has to be carried out anyway, because the initial frequency of the phase-locked loop, Ω_{ini} , must be set to a reasonable estimate of the linear natural frequency in order to track the intended backbone. This is true also in the case of the heuristic design. Besides, a linear modal test is generally advised for various reasons before any nonlinear test. For those reasons, it is not fair to count the effort for the linear modal test as additional preparation effort for the proposed design method. It is also interesting to note that the proposed design leads to a backbone test of about 10 s, while the linear modal test specified in Section 6.2 took about 90 s. The duration of the linear modal test depends on various parameters and could most certainly be reduced for the given purpose. Still, this comparison shows that the prevailing belief that nonlinear tests generally take longer than linear ones does no longer hold.

Fig. 11b compares online versus offline evaluation of the response. The online evaluation uses directly the output of the adaptive filter at the moment where the phase has locked. More precisely, the mean over the last period is taken, of the adaptive filter output (\hat{Q} , \hat{F}), and of the instantaneous frequency Ω . Hence, this technique does not require any hold times. As reference, the conventional technique is used, which relies on the recording of the hold times. More specifically, once the phase has locked, the voltage amplitude is held constant for 300 linear periods. Subsequently, the discrete Fourier transform is applied to the last 100 periods of the hold time.

The results of online and offline evaluation lie on the same backbone curve. The points are not perfectly identical, because the amplitude still evolves when the phase has locked. In contrast, the amplitude is expected to have settled before the last 100 periods of the hold time are reached. Note that an amplitude

settling detection can be implemented as well, in addition to the phase settling detection. It is useful to highlight that the 300 periods of hold time are much longer than the phase settling time achieved with the proposed controller design. As nearly identical curves are obtained, the online evaluation is regarded as valid. This justifies the proposed elimination of the hold times.

7. Conclusions

The overarching goal of the present work is to make backbone tracking robust and fast. We believe that the proposed approach is an important leap forward to reaching this goal. The key ingredients are an appropriate adaptive filter and an analytically designed proportional-integral controller. The adaptive filter permits to eliminate hold times. Thus, once the phase has locked, one can directly take the next step along the backbone, without the need to record a steady-state time span for post-processing. The adaptive filter also increases the robustness of the feedback loop, as compared to conventional phase detectors. For the same signal-to-noise ratio, higher cutoff frequency can be realized, which reduces the time scale of the phase transient. Thanks to the simple controller and reasonable model assumptions, a closed-form expression of the phase transient was possible. The proposed setting of the control gains is a well-defined trade-off between speed and robustness. An important benefit of the proposed approach is its easy implementation. The input for the design algorithm is obtained from shaker-based linear modal testing (usually done anyway before a nonlinear test), and an open-loop sine test at a single frequency and voltage level (to set the cutoff frequency of the adaptive filter). Also, thanks to the online evaluation, the post-processing effort is negligible. It is useful to emphasize that the approach is completely model-free, in the sense that no model of the exciter or the structure under test is required before the test. The numerical and experimental results demonstrate the excellent performance of the proposed approach. In particular, the controller parameters, which were designed for the linear regime, provide high speed and robustness also in the strongly nonlinear regime. Only ca. 100 vibration cycles were needed to reach a locked phase and obtain reliable data, for each backbone point. Thanks to the shorter test duration, consistent backbone tracking of slowly time-variable systems becomes feasible, and the structure under test is exposed to fewer cycles of high loading.

In spite of the excellent performance of the proposed approach, some optimization potential remains: First, in the present configuration, a constant cutoff frequency of the adaptive filter is used, which is determined for the lowest vibration level. With this, the noise present at the lowest vibration level dictates the duration of the entire backbone test. Thus, it seems useful and feasible to automatically adjust the cutoff frequency of the adaptive filter, along the backbone, as the signal-to-noise ratio varies. It would also be interesting to assess the potential of amplitude-adaptive control gains in the nonlinear regime (relying on amplitude-dependent modal properties). Further, the assumptions on the exciter could be relaxed (no phase-neutrality; higher dynamic exciter mass; more flexible stinger). The combination of the proposed phase controller with an amplitude controller, as mentioned at different occasions, is a natural extension, and the opportunity of an automatic step size adjustment should be explored. The generalization of the control design approach to phase stepping, in combination with excitation or response amplitude control, would be desirable. Finally, to gain further confidence in its wide applicability, the approach should be further assessed for a representative set of other challenging test rigs.

Acknowledgements

M. Krack is grateful for the funding received by the Deutsche Forschungsgemeinschaft (DFG, German Research Foundation) [Project 402813361].

Appendix A. Experimental identification of the linear modal data and the exciter parameters

The proposed control design approach summarized in Section 4.5, requires a few parameters related to the structure under test and the exciter. Those are the linear modal frequency of the structure under test, ω_{lin} , the decay rates δ_s and δ_p of the structure and plant, and the mass ratio μ_{ex} (again, assuming linear

behavior). Those quantities can be obtained from shaker-based linear modal testing, as explained in this appendix.

As stated in Section 2, it is assumed that the target modal frequency is well-separated, so that the near-resonant dynamics is dominated by a single mode, and Eq. 15 is valid. At steady state, $\dot{a} = 0 = \dot{v}$. In the linear regime, ω , D and φ_{ex} can be replaced by their linear counterparts ω_{lin} , D_{lin} and $\varphi_{\text{ex,lin}}$. From this, the frequency response of the *structure under test* (from applied force F to drive point response Q) can be derived:

$$\frac{Q}{F} = \frac{\varphi_{\text{ex,lin}}^2}{-\Omega^2 + 2\delta_s i\Omega + \omega_{\text{lin}}^2}. \quad (\text{A.1})$$

Herein, $Q = \varphi_{\text{ex,lin}} a e^{i\vartheta}$ is the fundamental Fourier coefficient of q_{ex} (drive point displacement). If the velocity or the acceleration is measured, Q can easily be obtained by integration in the frequency domain. Recall that $\delta_s = (D\omega)_{\text{lin}}$.

The frequency response function Q/F can be estimated by shaker-based testing in a range of the frequency Ω around the natural frequency of the target mode. From this frequency response function, $\varphi_{\text{ex,lin}}$, ω_{lin} and δ_s can be determined using a conventional modal parameter identification scheme. As the modal frequency is well-separated by assumption, simple single-degree-of-freedom techniques should give accurate results [33]. Substituting Eq. 16 into Eq. A.1, and solving for Q/U , one can derive the frequency response function of the *plant* (from voltage to drive point response):

$$\frac{Q}{U} = \frac{\varphi_{\text{ex,lin}}^2 \frac{G}{R}}{-\Omega^2 (1 + \mu_{\text{ex,lin}}) + 2\delta_p i\Omega + \omega_{\text{lin}}^2 + \mu_{\text{ex,lin}} \omega_{\text{ex}}^2}, \quad (\text{A.2})$$

$$= \frac{\frac{\varphi_{\text{ex,lin}}^2}{1 + \mu_{\text{ex,lin}}} \frac{G}{R}}{-\Omega^2 + 2\tilde{\delta} i\Omega + \tilde{\omega}^2}. \quad (\text{A.3})$$

Note that the frequency response function Q/U can be estimated based on the same test as that for Q/F . This transfer function should also be valid in the frequency band around ω_{lin} . One can identify $\tilde{\delta}$ and $\tilde{\omega}^2$ using the same modal identification method as before.

It is proposed to manually determine the moving mass of the exciter, m_{ex} . m_{ex} includes coil, shaker table, stinger, and the impedance head/force sensor. Subsequently, one can calculate $\mu_{\text{ex,lin}} = m_{\text{ex}} \varphi_{\text{ex,lin}}^2$, and obtain ω_{ex} , δ_p from

$$\omega_{\text{ex}}^2 = \frac{\tilde{\omega}^2 (1 + \mu_{\text{ex,lin}}) - \omega_{\text{lin}}^2}{\mu_{\text{ex,lin}}}, \quad (\text{A.4})$$

$$\delta_p = \tilde{\delta} (1 + \mu_{\text{ex,lin}}). \quad (\text{A.5})$$

If desired, one can also calculate $D_{\text{ex}} = (\delta_p - \delta_s) / \mu_{\text{ex,lin}}$ and $k_{\text{ex}} = m_{\text{ex}} \omega_{\text{ex}}^2$. An alternative is to directly identify the exciter parameters k_{ex} , d_{ex} , G , R , following, for instance [37], and to obtain the derived quantities ω_{ex} , δ_p .

Appendix B. Adaptive filter: from time discrete to time continuous form

Let $x(t_i)$ be a time discrete signal, sampled at equidistant times $t_{i+1} - t_i = T_s$, where T_s is the sampling time. We seek the Fourier decomposition of $x(t_i)$ for a given fundamental frequency Ω . More specifically, we wish to find the Fourier coefficients $\hat{X}^{(h)}$, $h = 0, \dots, H$, so that $x(t_i) \approx \hat{x}(t_i)$ with

$$\hat{x}(t_i) = \Re \left\{ \sum_{h=0}^H \hat{X}^{(h)} e^{ih\Omega t_i} \right\}. \quad (\text{B.1})$$

For simplicity, a constant Ω is considered in this appendix. The Widrow-Hoff LMS algorithm stated in Equation A.15 in [21] yields a simple update scheme,

$$\hat{X}^{(h)}(t_{i+1}) = \hat{X}^{(h)}(t_i) + 2\omega_{\text{LP}} T_s e^{-ih\Omega t_i} (x(t_i) - \hat{x}(t_i)) \quad h = 0, \dots, H. \quad (\text{B.2})$$

In the present work, we use harmonics, $e^{ih\Omega t_i}$, while the algorithm proposed in [21] is defined for arbitrary base signals. The update scheme in Eq. B.2 is an approximation to the least-squares minimization of the error $x(t_i) - \hat{x}(t_i)$ (least-mean-squares fit of Eq. B.1 to $x(t_i)$), hence the name LMS algorithm. Instead of the complex-exponential representation considered in the present work, one can of course use the equivalent sine-cosine representation.

Dividing Eq. B.2 by T_s on both sides, and regarding the limit of $T_s \rightarrow 0$, one obtains the ordinary differential equation

$$\dot{\hat{X}}^{(h)} = 2\omega_{\text{LP}} e^{-ih\Omega t} \left(x - \Re \left\{ \sum_{h=0}^H e^{ih\Omega t} \hat{X}^{(h)} \right\} \right) \quad h = 0, \dots, H. \quad (\text{B.3})$$

Applied to q_{ex} , f , and generalizing Ωt to τ , this yields Eqs. 5-6.

Appendix C. Additional derivations required for the proposed controller design

This appendix contains additional mathematical developments underlying the theory presented in Section 3. Appendix C.1 shows the reduction from the three real and two complex state variables a , ϑ , \hat{F} , \hat{Q} , I_ε to the four real state variables $\mathbf{z} = [a; \vartheta; \varepsilon; \bar{I}_\varepsilon]$. Appendix C.2 derives the linearization around the locked state. Appendix C.3 introduces the additional assumptions of a phase-neutral exciter and a linear behavior of the structure under test, in order to arrive at Eqs. 28-29. This permits to decouple the phase transient from the amplitude dynamics, which is an important simplification. Finally, Appendix C.4 solves the simplified, linear autonomous ordinary differential equation system for the case of an initial unit frequency error, and establishes the optimum setting of the control gains.

Appendix C.1. Reduction of state-space dimension in linearized case

As stated in Section 3.2, the dynamics of the closed loop on the slow time scale is described by a set of first-order ordinary differential equations Eq. 15, Eqs. 17-18, Eq. 11, with state variables a , ϑ , \hat{F} , \hat{Q} , I_ε . One can eliminate the two complex states, \hat{F} and \hat{U} , by introducing ε as state variable, as shown in the following. This is only possible in the linear case.

First, the polar transform $F = |F| e^{i\vartheta_f}$ is introduced, and analogous for \hat{F} . Substituting this into Eq. 17 yields

$$\begin{aligned} \dot{\hat{F}} &= \left(|\dot{\hat{F}}| + i\dot{\vartheta}_f |\hat{F}| \right) e^{i\hat{\vartheta}_f} \\ &= \omega_{\text{LP}} \left(|F| e^{i\vartheta_f} - |\hat{F}| e^{i\hat{\vartheta}_f} \right). \end{aligned} \quad (\text{C.1})$$

From this, one can obtain

$$\dot{\vartheta}_f = \omega_{\text{LP}} \frac{|F|}{|\hat{F}|} \sin(\vartheta_f - \hat{\vartheta}_f), \quad (\text{C.2})$$

$$\dot{\vartheta} = \omega_{\text{LP}} \frac{|Q|}{|\hat{Q}|} \sin(\vartheta - \hat{\vartheta}). \quad (\text{C.3})$$

Eq. C.3 follows analogously to the derivation of Eq. C.2 (by substituting the polar transform of $Q = a\varphi_{\text{ex}} e^{i\vartheta}$ and \hat{Q} into Eq. 18). By taking the time derivative of on both sides of Eq. 10, and exploiting that the reference phase $\frac{\pi}{2}$ is constant, one obtains

$$\begin{aligned} \dot{\varepsilon} &= -(\dot{\vartheta}_f - \dot{\vartheta}) \\ &= \omega_{\text{LP}} \left[\frac{|Q|}{|\hat{Q}|} \sin(\vartheta - \hat{\vartheta}) - \frac{|F|}{|\hat{F}|} \sin(\vartheta_f - \hat{\vartheta}_f) \right]. \end{aligned} \quad (\text{C.4})$$

This can be linearized about the fixed point $|F| = |\hat{F}|$, $|Q| = |\hat{Q}|$, $\vartheta = \hat{\vartheta}$, $\vartheta_f = \hat{\vartheta}_f$, $\varepsilon = 0$, with respect to a generic variable x :

$$\begin{aligned} \left. \frac{\partial \dot{\varepsilon}}{\partial x} \right|_{\text{FP}} &= \left[\omega_{\text{LP}} \frac{\partial}{\partial x} \left(\vartheta - \hat{\vartheta} - \vartheta_f + \hat{\vartheta}_f \right) \right] \Big|_{\text{FP}} \\ &= \left[\omega_{\text{LP}} \frac{\partial}{\partial x} \left(\vartheta - \vartheta_f + \frac{\pi}{2} - \varepsilon \right) \right] \Big|_{\text{FP}}. \end{aligned} \quad (\text{C.5})$$

Herein, $\square|_{\text{FP}}$ stands for evaluation at FP, where FP stands for farty pants in general, but for fixed point in this specific context. From the first to the second line in Eq. C.5, Eq. 10 was used.

Appendix C.2. Linearized ODEs around locked state

Thanks to Appendix C.1, the new state vector $\mathbf{z} = [a; \vartheta; \varepsilon; \bar{I}_\varepsilon]$ can be used. Recall that the normalized time is $\bar{t} = \omega_{\text{LP}} t$. Sufficiently small deviations $\Delta \mathbf{z}$ from the fixed point are governed by the linear ordinary differential equation system

$$\Delta \mathbf{z}' = \left. \frac{\partial \mathbf{f}}{\partial \mathbf{z}} \right|_{\text{FP}} \Delta \mathbf{z}, \quad (\text{C.6})$$

$$\mathbf{f}(\mathbf{z}) = \begin{bmatrix} f_1 \\ f_2 \\ f_3 \\ f_4 \end{bmatrix} = \begin{bmatrix} -\frac{D\omega + \mu_{\text{ex}} D_{\text{ex}} \omega_{\text{ex}}}{\omega_{\text{LP}}^2 + \mu_{\text{ex}} \omega_{\text{ex}}^2 - \Omega^2} a - \frac{GU \varphi_{\text{ex}}}{2\Omega \omega_{\text{LP}} R} \sin \vartheta \\ \frac{\omega^2 + \mu_{\text{ex}} \omega_{\text{ex}}^2 - \Omega^2 (1 + \mu_{\text{ex}})}{2\Omega \omega_{\text{LP}}} - \frac{GU \varphi_{\text{ex}}}{2\Omega \omega_{\text{LP}} a R} \cos \vartheta \\ \vartheta - \vartheta_f + \frac{\pi}{2} - \varepsilon \\ \varepsilon \end{bmatrix}, \quad (\text{C.7})$$

where Eq. C.6 is obtained by first-order Taylor series expansion of the initial nonlinear ordinary differential equation system around the fixed point. $a' = f_1$, $\vartheta' = f_2$ are obtained by substituting Eq. 16 into Eq. 15, splitting into real and imaginary parts, and solving explicitly for a and ϑ . $\varepsilon' = f_3$ is not valid. In fact, a function \tilde{f}_3 with $\varepsilon' = \tilde{f}_3$ can be inferred from Eq. C.4, but \tilde{f}_3 cannot be expressed as function of \mathbf{z} . However, the linearization of \tilde{f}_3 is equivalent to the linearization of f_3 , as shown by Eq. C.5. f_4 corresponds to Eq. 11, where $\bar{I}_\varepsilon = \omega_{\text{LP}} I_\varepsilon$. ϑ_f is the argument of $F = |F|e^{i\vartheta_f}$. Using Eq. 16 and recalling that $0 < \varphi_{\text{ex}} \in \mathbb{R}$, we have

$$\vartheta_f = \text{Arg} \left\{ \frac{\varphi_{\text{ex}} GU}{R} - (-\Omega^2 + 2i\Omega D_{\text{ex}} \omega_{\text{ex}} + \omega_{\text{ex}}^2) \mu_{\text{ex}} a e^{i\vartheta} \right\}. \quad (\text{C.8})$$

Using Eq. 9, Ω can be expressed as

$$\Omega = \Omega_{\text{ini}} + \omega_{\text{LP}} \bar{k}_{\text{p}} \varepsilon + \omega_{\text{LP}} \bar{k}_{\text{i}} \bar{I}_\varepsilon. \quad (\text{C.9})$$

Appendix C.3. Phase-neutral exciter and structure under test in linear regime

The assumption of a phase-neutral exciter specifically means that

$$\mu_{\text{ex}}(\omega_{\text{ex}}^2 - \omega^2) \approx 0. \quad (\text{C.10})$$

This condition holds if

- (a) $\mu_{\text{ex}} \approx 0$; i.e., the moving mass of the exciter is small and/or the exciter is attached far away from the vibration anti-node(s), and/or
- (b) $\omega_{\text{ex}}^2 \approx \omega^2$; i.e., structure and exciter are frequency-matched.

To achieve frequency matching, one should adjust the exciter stiffness rather than the exciter mass, otherwise one counteracts (a).

At the fixed point, we must have $f_1 = 0 = f_2$. Using Eq. 26, the first term of f_2 defined in Eq. C.7 vanishes under the above assumption. Recalling that we assumed $a, \varphi_{\text{ex}}, \omega, \omega_{\text{LP}}, U, G, R > 0$, this leads to

the condition $\cos \vartheta = 0$, which admits the two solutions $\vartheta = \pm\pi/2$ in the interval $\vartheta \in [-\pi, \pi[$. From $f_1 = 0$, one can derive that $\sin \vartheta < 0$ for positive damping ($D\omega + \mu_{\text{ex}}D_{\text{ex}}\omega_{\text{ex}} > 0$), i. e., $\vartheta \in [-\pi, 0[$. The only solution is thus $\vartheta = -\pi/2$. Taking into account Eq. 10, and Eqs. 24-25 at steady state, this implies that $\vartheta_f = 0$; i. e., the applied force has the same phase as the voltage at steady state. In an experiment, one can actually measure ϑ_f , to evaluate to what extent phase-neutrality is met for a given exciter-structure configuration. For a point in the linear regime of the structure under test, D , ω , φ_{ex} , μ_{ex} are constant; i. e., their derivative with respect to a vanishes. The computation of the remaining derivatives is straight forward for most states. The third row (phase error ε), however, requires additional care since it involves derivatives of the phase lag of the excitation force against the reference (voltage), ϑ_f . To compute those derivatives, we first express

$$\vartheta_f = \arctan \left(\frac{\Im \{F\}}{\Re \{F\}} \right) \quad (\text{C.11})$$

with

$$\Re \{F\} = \frac{\varphi_{\text{ex}}GU}{R} + \left(-(\Omega^2 + \omega_{\text{ex}}^2) \cos \vartheta + 2\Omega D_{\text{ex}}\omega_{\text{ex}} \sin \vartheta \right) \mu_{\text{ex}}a \quad (\text{C.12})$$

$$\Im \{F\} = (2\Omega D_{\text{ex}}\omega_{\text{ex}} \cos \vartheta + (-\Omega^2 + \omega_{\text{ex}}^2) \sin \vartheta) \mu_{\text{ex}}a. \quad (\text{C.13})$$

Note that Eq. C.11 is only valid if the phase of the force is within $[-\pi/2, \pi/2]$. Since the linearization in this work is done under the assumption of a phase-neutral exciter, i. e. $\vartheta_f \approx 0$, this is not considered a relevant restriction. By computing the derivatives, inserting the fixed-point values, and after some algebraic manipulations, one eventually obtains Eqs. 28-29.

Appendix C.4. Analytical solution of the linearized closed-loop system

First, we establish the relations between the eigenvalues λ_1 , λ_2 , λ_3 , defined in Eqs. 38-40, and the control gains. Thanks to the decoupling from the amplitude dynamics, it is useful to isolate the equations governing the phase in Eqs. 28-29

$$\Delta \mathbf{y}' = \mathbf{B}_0 \Delta \mathbf{y}, \quad (\text{C.14})$$

$$\mathbf{B}_0 = \begin{bmatrix} -\bar{\delta}_{\text{p}} & -\bar{k}_{\text{p}} & -\bar{k}_{\text{i}} \\ \frac{\delta_{\text{p}}}{\delta_{\text{s}}} & -1 & 0 \\ 0 & 1 & 0 \end{bmatrix}, \quad (\text{C.15})$$

where $\Delta \mathbf{y} = [\vartheta; \varepsilon; \bar{I}_{\varepsilon}]$. We now consider the characteristic polynomial of \mathbf{B}_0 ,

$$0 = \lambda^3 + (\bar{\delta}_{\text{p}} + 1) \lambda^2 + \bar{\delta}_{\text{p}} \lambda + (\bar{k}_{\text{i}} + \bar{k}_{\text{p}} \lambda) \frac{\delta_{\text{p}}}{\delta_{\text{s}}} \quad (\text{C.16})$$

$$= (\lambda - \lambda_{\text{R}}) (\lambda - \lambda_{\text{R}} - \text{i} \lambda_{\text{I}}) (\lambda - \lambda_{\text{R}} + \text{i} \lambda_{\text{I}}). \quad (\text{C.17})$$

By comparing the coefficient of λ^2 in the first and the second row, one can verify Eq. 37. Analogously, for the linear and the constant term, one can solve for the dimensionless control gains \bar{k}_{p} , \bar{k}_{i} . This yields Eqs. 41-42.

The general solution of Eq. 28, under consideration of Eqs. 38-40 is

$$\Delta y(\bar{t}) = c_1 \boldsymbol{\psi}_1 e^{\lambda_{\text{R}} \bar{t}} + \left(c_2 \boldsymbol{\psi}_2 e^{(\lambda_{\text{R}} + \text{i} \lambda_{\text{I}}) \bar{t}} + \text{c.c.} \right), \quad (\text{C.18})$$

where c.c. stands for the complex-conjugate of the term in the parenthesis before, and $c_1 \in \mathbb{R}$ while $c_2 \in \mathbb{C}$. The eigenvectors $\boldsymbol{\psi}_1$, $\boldsymbol{\psi}_2$ can be obtained from the rank deficient linear algebraic equation system $(\lambda_{\nu} \mathbf{I} - \mathbf{B}_0) \boldsymbol{\psi}_{\nu} = \mathbf{0}$, as

$$\boldsymbol{\psi}_1 = \begin{bmatrix} (-\bar{\delta}_{\text{p}} + 2) (\bar{\delta}_{\text{p}} + 1) \\ 3 \frac{\delta_{\text{p}}}{\delta_{\text{s}}} (\bar{\delta}_{\text{p}} + 1) \\ -9 \frac{\delta_{\text{p}}}{\delta_{\text{s}}} \end{bmatrix}, \quad \boldsymbol{\psi}_2 = \begin{bmatrix} (-\bar{\delta}_{\text{p}} + 2 + 3\text{i} \lambda_{\text{I}}) (\bar{\delta}_{\text{p}} + 1 - 3\text{i} \lambda_{\text{I}}) \\ 3 \frac{\delta_{\text{p}}}{\delta_{\text{s}}} (\bar{\delta}_{\text{p}} + 1 + 3\text{i} \lambda_{\text{I}}) \\ -9 \frac{\delta_{\text{p}}}{\delta_{\text{s}}} \end{bmatrix}, \quad (\text{C.19})$$

where an arbitrary scaling was used. Note that ψ_1 is real and ψ_2 is complex.

As explained in Section 3.3, we wish to optimize the settling of the phase transient, from steady state (phase resonance $\Delta\vartheta = 0$, no control error $\Delta\varepsilon = 0$) for an initial frequency error. Recalling Eq. C.9, we can introduce the non-dimensional frequency error $\Delta\bar{\Omega} = \Delta\Omega/\omega_{\text{LP}}$

$$\Delta\bar{\Omega}(\bar{t}) = \bar{k}_p \Delta\varepsilon(\bar{t}) + \bar{k}_i \Delta\bar{I}_\varepsilon(\bar{t}). \quad (\text{C.20})$$

Since $\Delta\varepsilon(0) = 0$, the initial frequency error corresponds to an initial value $\Delta\bar{I}_\varepsilon(0) \neq 0$. Since the problem is linear, the initial frequency error can be arbitrarily scaled. For a unit frequency error, $\Delta\bar{\Omega}(0) = 1$, we obtain $\Delta\bar{I}_\varepsilon(0) = 1/\bar{k}_i$.

The coefficients c_1, c_2 follow from the linear algebraic equation system

$$\begin{bmatrix} \psi_1 & \Re\{\psi_2\} & -\Im\{\psi_2\} \end{bmatrix} \begin{bmatrix} c_1 \\ c_{2,\text{R}} \\ c_{2,\text{I}} \end{bmatrix} = \begin{bmatrix} 0 \\ 0 \\ \frac{1}{\bar{k}_i} \end{bmatrix}, \quad (\text{C.21})$$

where $c_{2,\text{R}}, c_{2,\text{I}}$ are real and imaginary parts of c_2 . The solution is

$$c_1 = -\frac{1}{9\bar{k}_i} \frac{\delta_s}{\delta_p} \left(1 + \frac{\lambda_{\text{R}}^2}{\lambda_{\text{I}}^2} \right), \quad (\text{C.22})$$

$$c_2 = \frac{1}{18\bar{k}_i} \frac{\delta_s}{\delta_p} \frac{\lambda_{\text{R}}}{\lambda_{\text{I}}} \left(3 \frac{\lambda_{\text{R}}}{\lambda_{\text{I}}} - i \right). \quad (\text{C.23})$$

After insertion into Eq. C.18 and some algebraic manipulations, one obtains

$$\Delta\varepsilon(\bar{t}) = \frac{\lambda_{\text{R}}}{\bar{k}_i} \left(1 + \frac{\lambda_{\text{R}}^2}{\lambda_{\text{I}}^2} \right) e^{\lambda_{\text{R}}\bar{t}} (1 - \cos(\lambda_{\text{I}}\bar{t})), \quad (\text{C.24})$$

$$\Delta\bar{I}_\varepsilon(\bar{t}) = \frac{1}{\bar{k}_i} e^{\lambda_{\text{R}}\bar{t}} \left(\left(1 + \frac{\lambda_{\text{R}}^2}{\lambda_{\text{I}}^2} \right) - \frac{\lambda_{\text{R}}}{\lambda_{\text{I}}} \left(\frac{\lambda_{\text{R}}}{\lambda_{\text{I}}} \cos(\lambda_{\text{I}}\bar{t}) + \sin(\lambda_{\text{I}}\bar{t}) \right) \right). \quad (\text{C.25})$$

For positive damping, the phase error (Eq. C.24) starts at zero and then becomes negative (positive for $\Delta\bar{\Omega}(0) < 0$). Due to the overall decay, the first local minimum is the largest deviation from the target value zero (cf. Fig. 3a). By setting the derivative of Eq. C.24 to zero and solving for \bar{t} one can identify possible extreme values of the phase error at times

$$\bar{t} = \frac{n2\pi}{\lambda_{\text{I}}} \quad \text{and} \quad \bar{t} = \frac{2}{\lambda_{\text{I}}} \left(n\pi - \arctan \frac{\lambda_{\text{I}}}{\lambda_{\text{R}}} \right), \quad n \in \mathbb{Z}. \quad (\text{C.26})$$

Since $\lambda_{\text{R}} < 0$ and $\lambda_{\text{I}} > 0$ (by definition), the arctan function in Eq. C.26 returns values in $] -\frac{\pi}{2}, 0[$. Thus, the smallest positive time with horizontal tangent of ε is

$$\bar{t}_\varepsilon = -\frac{2}{\lambda_{\text{I}}} \arctan \frac{\lambda_{\text{I}}}{\lambda_{\text{R}}}. \quad (\text{C.27})$$

One can check that $\varepsilon''(\bar{t}_\varepsilon) > 0$; i.e. \bar{t}_ε is indeed the sought minimum.

By inserting \bar{t}_ε in Eq. C.24 one finds the largest absolute value of the phase error,

$$|\Delta\varepsilon|_{\text{max}} = |\Delta\varepsilon(\bar{t}_\varepsilon)| = \frac{1}{\omega_{\text{LP}}} \frac{\delta_p}{\delta_s} \frac{2}{\lambda_{\text{R}}^2 + \lambda_{\text{I}}^2} e^{-2\frac{\lambda_{\text{R}}}{\lambda_{\text{I}}} \arctan \frac{\lambda_{\text{I}}}{\lambda_{\text{R}}}}, \quad (\text{C.28})$$

as function of λ_{I} .

The frequency error starts at 1 and then decreases. The first local minimum is again the largest deviation from the target value zero (cf. Fig. 3b). The corresponding times can be identified as before:

$$\bar{t} = \frac{n2\pi}{\lambda_{\text{I}}} \quad \text{and} \quad \bar{t} = \frac{2}{\lambda_{\text{I}}} (n\pi - \arctan \eta), \quad n \in \mathbb{Z}, \quad (\text{C.29})$$

with the auxiliary variable $\eta = \frac{\lambda_I(\lambda_I^2 + 3\lambda_R^2 - \bar{\delta}_p)}{\lambda_R(\lambda_R^2 - \bar{\delta}_p)}$. One can find that $\eta(\bar{\delta}_p)$ changes its sign for $\lambda_I = 1/2$ and for $\lambda_I = 2$, where also the sign of η changes. Since η is used as argument of the arctan function of in Eq. C.29, a case distinction is necessary. The smallest possible time at which an extreme value occurs, is

$$\bar{t}_\Omega = \frac{2}{\lambda_I} (n\pi - \arctan \eta) \quad n = \begin{cases} 0, \bar{\delta}_p > \frac{1}{2} \text{ or } \bar{\delta}_p > 2 \\ 1, \frac{1}{2} < \bar{\delta}_p < 2 \end{cases} . \quad (\text{C.30})$$

Inserting this into Eq. C.20 yields the largest absolute frequency overshoot,

$$|\Delta\bar{\Omega}|_{\max} = |\Delta\bar{\Omega}(\bar{t}_\Omega)| = \frac{1}{\omega_{LP}} \frac{1}{\lambda_R^2 + \lambda_I^2} e^{2\frac{\lambda_R}{\lambda_I}(n\pi - \arctan \eta)} \left[\left(1 + \frac{\lambda_R^2}{\lambda_I^2}\right) (2\lambda_R^2 - \bar{\delta}_p) + \right. \quad (\text{C.31})$$

$$\left. \left(\left(1 + \frac{\lambda_R^2}{\lambda_I^2}\right) (-2\lambda_R^2 + \bar{\delta}_p) - \lambda_R^2 - \lambda_I^2 \right) \frac{1 - \eta^2}{1 + \eta^2} - \lambda_R \left(\frac{\lambda_R^2}{\lambda_I^2} + \lambda_I \right) \frac{2\eta}{1 + \eta^2} \right], \quad (\text{C.32})$$

as function of λ_I .

The maximum phase error goes to zero for $\lambda_I \rightarrow \infty$, while the largest phase error is obtained in the limit case of $\lambda_I \rightarrow 0$:

$$|\Delta\varepsilon|_{\max,0} = \frac{1}{\omega_{LP}} \frac{\delta_p}{\delta_s} \frac{2}{\lambda_R^2} e^{-2} . \quad (\text{C.33})$$

On the other hand, the frequency overshoot goes to zero for $\lambda_I \rightarrow 0$, while the largest frequency overshoot is obtained in the limit case of $\lambda_I \rightarrow \infty$, which equals the initial value 1. The optimum λ_I is proposed as a trade-off, for which the control error and frequency overshoot, normalized by their respective limit values, are minimized. This can be expressed as the condition

$$\frac{|\Delta\varepsilon|_{\max}}{|\Delta\varepsilon|_{\max,0}} = \frac{|\Delta\bar{\Omega}|_{\max}}{1} , \quad (\text{C.34})$$

recalling that a unity initial frequency error was considered. Eq. C.34 has to be solved for λ_I . Since the equation is transcendent, a closed-form solution is not available. As it turns out, left- and right-hand side depend only on λ_I and $\bar{\delta}_p$. Note that λ_R depends explicitly on $\bar{\delta}_p$ (Eq. 37); ω_{LP} and δ_p/δ_s cancel thanks to the normalization by the respective limit value. Indeed, there is a unique solution to Eq. C.34 for each $\bar{\delta}_p$; i. e., there is a solution curve $\lambda_I(\bar{\delta}_p)$ which is plotted in Fig. 4.

References

- [1] D. J. Ewins, *Modal Testing: Theory and Practice*. Taunton: Research Studies Press Ltd., 1995.
- [2] P. A. Atkins, J. R. Wright, and K. Worden, “An extension of force appropriation to the identification of non-linear multi-degree of freedom systems,” *Vibro-Impact Systems*, vol. 237, no. 1, pp. 23–43, 2000.
- [3] M. Peeters, G. Kerschen, and J. C. Golinval, “Dynamic testing of nonlinear vibrating structures using nonlinear normal modes,” *Journal of Sound and Vibration*, vol. 330, no. 3, pp. 486–509, 2011.
- [4] M. Peeters, G. Kerschen, and J. C. Golinval, “Modal testing of nonlinear vibrating structures based on nonlinear normal modes: Experimental demonstration,” *Mechanical Systems and Signal Processing*, vol. 25, no. 4, pp. 1227–1247, 2011.
- [5] M. Krack, “Nonlinear modal analysis of nonconservative systems: Extension of the periodic motion concept,” *Computers and Structures*, vol. 154, pp. 59–71, 2015.
- [6] M. Scheel, S. Peter, R. I. Leine, and M. Krack, “A phase resonance approach for modal testing of structures with nonlinear dissipation,” *Journal of Sound and Vibration*, vol. 435, pp. 56–73, 2018.
- [7] F. Müller, L. Woiwode, J. Gross, M. Scheel, and M. Krack, “Nonlinear damping quantification from phase-resonant tests under base excitation,” *Mechanical Systems and Signal Processing*, 2022.
- [8] L. Renson, T. L. Hill, D. A. Ehrhardt, D. A. W. Barton, and S. A. Neild, “Force appropriation of nonlinear structures,” *Proceedings of the Royal Society A: Mathematical, Physical and Engineering Sciences*, vol. 474, no. 2214, p. 20170880, 2018.
- [9] R. J. Kuether, L. Renson, T. Detroux, C. Grappasonni, G. Kerschen, and M. S. Allen, “Nonlinear normal modes, modal interactions and isolated resonance curves,” *Journal of Sound and Vibration*, vol. 351, pp. 299–310, 2015.

- [10] L. Woiwode and M. Krack, "Experimentally uncovering isolas via backbone tracking," *Journal of Structural Dynamics*, no. 2, pp. 122–143, 2024.
- [11] I. J. Sokolov and V. I. Babitsky, "Phase control of self-sustained vibration," *Journal of Sound and Vibration*, vol. 248, no. 4, pp. 725–744, 2001.
- [12] Sebastian Mojrzisch, Jörg Wallaschek, and Jan Bremer, "An experimental method for the phase controlled frequency response measurement of nonlinear vibration systems," *PAMM*, vol. 12, no. 1, pp. 253–254, 2012.
- [13] M. Scheel, "Nonlinear modal testing of damped structures: Velocity feedback vs. phase resonance," *Mechanical Systems and Signal Processing*, vol. 165, 2022.
- [14] L. Renson, A. Gonzalez-Buelga, D. Barton, and S. Neild, "Robust identification of backbone curves using control-based continuation," *Journal of Sound and Vibration*, vol. 367, pp. 145–158, 2016.
- [15] G. Abeloos, F. Müller, E. Ferhatoglu, M. Scheel, C. Collette, G. Kerschen, M. Brake, P. Tiso, L. Renson, and M. Krack, "A consistency analysis of phase-locked-loop testing and control-based continuation for a geometrically nonlinear frictional system," *Mechanical Systems and Signal Processing*, vol. 170, p. 108820, 2022.
- [16] P. Axelsson and A. Johnsson, "Phase-locked loop technique to record resonance frequency of plant tissue," *Physiologia Plantarum*, vol. 36, no. 2, pp. 113–117, 1976.
- [17] J. A. Connally and S. B. Brown, "Micromechanical fatigue testing," *Experimental Mechanics*, vol. 33, no. 2, pp. 81–90, 1993.
- [18] V. Denis, M. Jossic, C. Giraud-Audine, B. Chomette, A. Renault, and O. Thomas, "Identification of nonlinear modes using phase-locked-loop experimental continuation and normal form," *Mechanical Systems and Signal Processing*, vol. 106, no. 3, pp. 430–452, 2018.
- [19] S. Peter and R. I. Leine, "Excitation power quantities in phase resonance testing of nonlinear systems with phase-locked-loop excitation," *Mechanical Systems and Signal Processing*, vol. 96, no. April, pp. 139–158, 2017.
- [20] J. Twiefel, M. Klubal, C. Paiz, S. Mojrzisch, and H. Krüger, "Digital signal processing for an adaptive phase-locked loop controller," in *Modeling, Signal Processing, and Control for Smart Structures 2008* (D. K. Lindner, ed.), SPIE Proceedings, p. 69260A, SPIE, 2008.
- [21] B. Widrow, J. R. Glover, J. M. McCool, J. Kaunitz, C. S. Williams, R. H. Hearn, J. R. Zeidler, Eugene Dong JR., and R. C. Goodlin, "Adaptive noise cancelling: Principles and applications," *Proceedings of the IEEE*, vol. 63, no. 12, pp. 1692–1716, 1975.
- [22] B. Widrow, P. Baudrenghien, M. Vetterli, and P. Titchener, "Fundamental relations between the lms algorithm and the dft," *IEEE transactions on circuits and systems*, vol. 34, no. 7, pp. 814–820, 1987.
- [23] G. Abeloos, L. Renson, C. Collette, and G. Kerschen, "Stepped and swept control-based continuation using adaptive filtering," *Nonlinear Dynamics*, vol. 104, no. 4, pp. 3793–3808, 2021.
- [24] G. Abeloos, *Control-based methods for the identification of nonlinear structures*. PhD thesis, ULiège - Université de Liège [Sciences Appliquées], Liège, Belgium and F.R.S.-FNRS - Fonds de la Recherche Scientifique [BE], 24 November 2022.
- [25] X. Sun, R. Horowitz, and K. Komvopoulos, "Stability and resolution analysis of a phase-locked loop natural frequency tracking system for mems fatigue testing," *Journal of Dynamic Systems, Measurement, and Control*, vol. 124, no. 4, pp. 599–605, 2002.
- [26] M. Fan, M. Clark, and Z. C. Feng, "Implementation and stability study of phase-locked-loop nonlinear dynamic measurement systems," *Communications in Nonlinear Science and Numerical Simulation*, vol. 12, no. 7, pp. 1302–1315, 2007.
- [27] M. Feldman, "Hilbert transform in vibration analysis," *Mechanical Systems and Signal Processing*, vol. 25, no. 3, pp. 735–802, 2011.
- [28] J.-L. Dion, G. Chevallier, and N. Peyret, "Improvement of measurement techniques for damping induced by micro-sliding," *Mechanical Systems and Signal Processing*, vol. 34, no. 1-2, pp. 106–115, 2013.
- [29] J. M. Londoño, S. A. Neild, and J. E. Cooper, "Identification of backbone curves of nonlinear systems from resonance decay responses," *Journal of Sound and Vibration*, vol. 348, pp. 224–238, 2015.
- [30] B. J. Deaner, M. S. Allen, M. J. Starr, D. J. Segalman, and H. Sumali, "Application of viscous and iwan modal damping models to experimental measurements from bolted structures," *Journal of Vibration and Acoustics*, vol. 137, no. 2, pp. 021012–021012–12, 2015.
- [31] T. Karaağaçlı and H. N. Özgüven, "Experimental modal analysis of nonlinear systems by using response-controlled stepped-sine testing," *Mechanical Systems and Signal Processing*, vol. 146, p. 107023, 2021.
- [32] G. R. Tomlinson, "Force distortion in resonance testing of structures with electro-dynamic vibration exciters," *Journal of Sound and Vibration*, vol. 63, no. 3, pp. 337–350, 1979.
- [33] K. G. McConnell and P. S. Varoto, *Vibration testing: Theory and practice*. Hoboken, New Jersey: John Wiley & Sons Inc, second edition ed., 2008.
- [34] M. Krack, L. Panning-von Scheidt, and J. Wallaschek, "On the computation of the slow dynamics of nonlinear modes of mechanical systems," *Mechanical Systems and Signal Processing*, vol. 42, no. 1-2, pp. 71–87, 2014.
- [35] A. Hurwitz, "Ueber die bedingungen, unter welchen eine gleichung nur wurzeln mit negativen reellen theilen besitzt," *Mathematische Annalen*, vol. 46, no. 2, pp. 273–284, 1895.
- [36] F. Müller, M. W. Beck, and M. Krack, "Experimental validation of a model for a self-adaptive beam–slider system," *Mechanical Systems and Signal Processing*, vol. 182, p. 109551, 2023.
- [37] L. Della Flora and H. A. Gründling, "Time domain sinusoidal acceleration controller for an electrodynamic shaker," *IET Control Theory & Applications*, vol. 2, no. 12, pp. 1044–1053, 2008.